A Novel Change Detection Framework in Urban Area Using Multilevel Matching Feature and Automatic Sample Extraction Strategy

Yuanxiu Zhou, Yan Song, Songxue Cui, Haitian Zhu, Jie Sun, and Wenjun Qin

***Abstract*—Urban change detection (CD) using remote sensing images is of great significance for monitoring and analyzing the spatial and temporal distribution of changes within cities, which can be used to guide urban management. In order to reduce false detections and improve the CD automation, a novel CD framework for high resolution images is proposed in this article. First, a novel multilevel matching feature is presented, combining structural invariant features with multiscale dense matching features to comprehensively describe the invariant properties of ground objects at different levels. Second, a newly automatic training sample extraction strategy is proposed, in which sufficient and accurate no-change samples can be obtained by Gaussian-weighted Dempster–Shafer evidence theory and L1-norm, meanwhile, typical change samples can be extracted by sequential spectral change vector analysis. Utilizing the automatic extracted samples, the final CD results are obtained using four supervised classifiers, respectively (*k*-nearest neighbor, support vector machine, rotation forest, and extra-trees). To validate the proposed CD framework, experiments are conducted in four datasets with spectral variability, spectral confusion between the changed objects and unchanged backgrounds, and misregistration. The results demonstrate that the proposed multilevel matching feature and automatic sample extraction strategy can obtain better results with different types of supervised classifiers, and can effectively improve automation of CD, which is applicable to the large spatial extent scene.**

***Index Terms*—Automatic sample extraction strategy, change detection (CD), Gaussian-weighted Dempster–Shafer evidence theory, high resolution image, multilevel matching feature, sequential spectral change vector analysis.**

I. Introduction

REMOTE sensing (RS) Earth observation technology, which can provide high resolution (HR) image data sources with abundant detailed earth surface information, enables observation, identification, mapping, assessment, and monitoring of land cover at a range of spatial, temporal, and thematic scales [1], [2]. With the development of spacecraft and sensor technology, the multiview, multiscale, multisensor Earth observation satellite systems have been gradually established from moderate resolution to HR, which can ensure comprehensive and multidimensional monitoring for urban natural resource management.

Compared with the coarse and moderate resolution images, HR remote sensing images take the advantages of significant spatial resolution, which can present more detailed information and the evident internal structure of ground objects to achieve fine change detection (CD) in urban areas. These urban changes monitoring information [3]–[6] is important for analyzing the pressure on the natural ecosystem of increasing land use demand, indicating changes in environmental quality, such as the impact of urbanization on surface runoff, urban heat island effects, etc. Besides, it is essential for smart city, urban and rural development, and sustainable development.

Urban changes are characterized by multiscale and diverse categories. Specifically, urban land use can be grouped into two categories: Construction land and nonconstruction land. The processes of industrialization and urbanization are mainly reflected by the transition between construction land and nonconstruction land, and the structural changes within the construction land. Including large-scale changes in infrastructure construction, intensive industrial parks, and urban-rural settlement development introduced by urban expansion, as well as small-scale changes introduced by urban internal development such as roof repairs and temporary material stockpiles. Therefore, it is difficult to completely describe the changed properties of ground objects in urban areas.

In the CD process, the spectral variability within ground object is a crucial factor affecting detection accuracy. And with the increase of spatial resolution, the spectral variability of ground objects increases [7], [8], resulting in the phenomenon of "same object with different spectrum, different objects with same spectrum" becoming more and more serious. As a result, the CD methods only using spectral information cannot detect the change information correctly and will lead to a lot of false alarms. In order to solve the problems, different feature extraction methods have been applied in CD.

Manuscript received January 2, 2021; revised February 5, 2021; accepted February 20, 2021. Date of publication March 8, 2021; date of current version April 21, 2021. This work was supported in part by the Satellite High Resolution Infrared Hyperspectral Camera and Application Technology under Grant D040104, "The 13th Five-Year Plan" in Space Advance Research Project for Civilian Application, in part by the Integration and Application Demonstration in the Marine Field under Grant 2020010004, and in part by the Automated Identifying of Environment Changes Using Satellite Time-Series, Dragon 5 Cooperation 2020–2024 (57971). *(Corresponding author: Yan Song.)*

Yuanxiu Zhou, Yan Song, Jie Sun, and Wenjun Qin are with the School of Geography and Information Engineering, China University of Geosciences (Wuhan), Wuhan 430074, China (e-mail: zhouyuanxiu95@163.com; songyan@cug.edu.cn; jiesun@cug.edu.cn; 2324122413@qq.com).

Songxue Cui and Haitian Zhu are with the National Satellite Ocean Application Service, Beijing 100081, China, and also with the Key Laboratory of Space Ocean Remote Sensing and Application, Ministry of Natural Resources, Beijing 100081, China (e-mail: cuisongxue@163.com; zht@mail.nsoas.org.cn).

Digital Object Identifier 10.1109/JSTARS.2021.3064311

The features describing the spatial dependence relations between adjacent pixels have been presented to improve the separability of changes and no-changes, such as fusing spectral information with adjacent pixels [9], constructing an adaptive region [10], morphological attributes [11]–[13], gray-level co-occurrence matrix (GLCM) [14]–[16], Gabor features [17], [18], etc. Furthermore, object-oriented features have been complemented to spectral information by directly providing contextual and spatial features such as shape, texture, etc., which can reduce the effect of spectral variability, misregistration, and acquisition characteristics and have been investigated for HR images to extract change information [19]–[21].

Besides, features with scale invariance, such as scale-invariant feature transformation (SIFT) [22], speeded up robust features (SURF) [23], etc., have been applied in CD. Specifically, changes have been extracted by fusing SIFT point-wise approach and graph theory [24]. A method based on the SIFT algorithm and a contrario approach has been proposed, which can deal with multiresolutions, multisensors, and multiincidence angles situations [25]. Land-cover CD method with scale invariant by using spatial voting weighting method to fuse the detection results of maximally stable external region and SIFT algorithms has been proposed [26]. However, it should be noted that most extracted keypoints are positioned on fine structures, but very sparsely on homogeneous zones [24]. In addition, the extracted corresponding points or regions can directly describe the invariant information, while the unmatched regions may be caused by shadows, occlusions, or low local signal-to-noise ratio, which cannot be considered as changed regions directly.

According to the availability of training samples, CD methods can be divided into unsupervised methods and supervised methods [27], [28]. The unsupervised methods compare bi-temporal images directly to obtain the change information without any prior information, including thresholding [29], [30], change vector analysis (CVA) [31], [32], sequential spectral change vector analysis (S^2CVA) [33], [34], and Markov random field-based algorithm [35], [36], which have been widely used in land use/cover change monitoring. However, their performance is affected by several external factors, such as illumination variations, changes of atmospheric conditions, and poor sensor calibration [20]. In addition, unsupervised OBCD methods using HR image hinder the accuracy of CD due to insufficient comparison units in the fixed experimental areas [37].

The supervised CD methods utilize the learning ability of classifiers to extract change information, which are robust in dealing with changes in various illumination and atmospheric conditions at different imaging times [20], [38].

A sufficient number of training samples and their representativeness are critical for supervised methods [39]–[41], which label samples by field investigation and visual interpretation. And it is time-consuming and labor-intensive, limiting the application of supervised methods and reducing the degree of automation. Therefore, highly automated CD methods are required for large volume data processing and analysis [19], [42]. Semisupervised methods combine a large amount of unlabeled data and a small amount of labeled data in the training stage, which can be trained more accurately and efficiently, such as active learning [43], semisupervised learning on graph [44], and enhanced metric learning [9]. Some automatic training samples extraction methods have been presented, such as utilizing two threshold ranges instead of one threshold [21], conducting saliency detection, and extraction morphological building index on difference images to generate training sets [13]. However, the above methods have their own application scenarios.

The performance of classifiers are important factors affecting the accuracy of the supervised CD method. And there is a general agreement that the selection of a suitable classifier is still a problem due to the diversity sources, spatial resolution, training sets, and features [41], [45], etc. Many statistical and machine learning methods have been applied to CD and classification, including k-nearest neighbor (KNN) [46], [47], extra-trees (ExT) [48], support vector machine (SVM) [49], rotation forest (RoF) [15], [50], etc. However, different classifiers have their own merits, and it is difficult to answer which classifier is suitable for a specific study [41]. In addition, deep neural networks (DNNs) have improved the accuracy of CD [51]–[57], which can extract abstract semantic features of the ground objects from massive data automatically and hierarchically [58] depending on datasets. Currently, there are some freely available datasets for CD, but the amount of open datasets is small, and some of them have small data sizes [51].

From the above overview, in the CD process using HR data, due to the characteristics of HR images and differences in imaging conditions, the spectral variability of ground objects increases and the separability of changes and no-changes reduces, resulting in a large number of false detections in classical CD methods. Besides, a strategy for automatically extracting accurate and representative training samples is required to improve the CD automation and accuracy according to the feature space and the complexity of urban scenario.

Therefore, a novel CD framework is proposed in this article. First, a multilevel matching feature for CD is presented. It combines classical structural invariant features with multiscale dense matching features to provide a comprehensive description of the matching properties of ground objects at different levels, which can effectively improve the separability between changes and no-changes. Second, an automatic training sample extraction strategy is proposed. Based on the ability of the proposed features to describe invariant properties of ground objects, Gaussian-weighted D–S evidence theory, and L1-norm are applied to fuse multilevel matching features, which can reduce the uncertainty of unchanged property and directly extract a large number of accurate no-change samples. After that, combining the spectral and texture features, this article presents a multiple change sample extraction strategy based on S^2CVA, which can avoid the loss of some subtle changes due to information compression and extract typical change samples. Finally, to demonstrate the validity and applicability of the proposed features and sample extraction strategy, four representative classifiers (KNN, SVM, RoF, and ExT) are trained on the extracted samples to obtain final CD results.

In order to verify the effectiveness of the proposed method, four HR datasets are selected for experiments, and the proposed method is compared with traditional pixel-based CD methods.

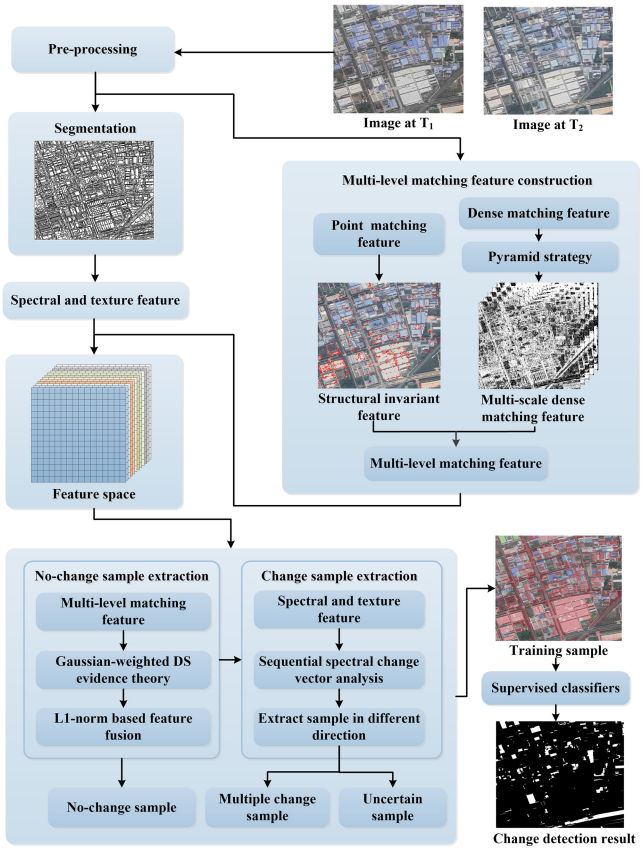

Fig. 1. Flowchart of the proposed CD method.

The rest of this article is structured as follows: The proposed CD framework is proposed in Section II. The experimental results and discussion are presented in Section III. Finally, Section IV concludes this article.

II. Methodology

To solve the problems and difficulties of urban CD with HR images, a novel CD framework is proposed in this article. The flowchart is shown in Fig. 1.

1) Based on multitemporal stacked images, an object-oriented segmentation is performed to obtain the object as the analysis unit, which can better preserve the contiguous of regions and effectively reduce small spurious changes by smoothing process [20].
2) A novel multilevel matching feature combining the structural invariant feature with multiscale dense matching feature is proposed and investigated with spectral and texture features to construct the feature space.
3) A large number of accurate no-change samples are obtained automatically by fusing multilevel matching features with Gaussian-weighted D–S evidence theory and L1-norm. Based on spectral and textural features, the S^2CVA method is used to extract multiple change samples automatically.
4) Four classical supervised classifiers are applied to conduct the final CD.

Fig. 2. Regions with structural invariant property. (a) Correspondences in T_1 image. (b) Correspondences in T_2 image.

A. Multilevel Matching Feature

In the process of CD using HR images, the separability of changes and no-changes is reduced due to the spectral variability. The traditional CD method with spectral and texture features will result in a lot of false alarms. Hence, on the basis of spectral and texture features, a multilevel matching feature is proposed in this article to solve the problems above and improve the CD accuracy. The multilevel matching feature combines structural invariant feature and multiscale dense matching feature to measure the possibility of no-changes, which can comprehensively represent invariant property from structure and scale level.

1) Structural Invariant Feature: Stable local features like SIFT, SURF, which can capture and present the local geometric structure of images, have been used for CD [24]–[26]. SIFT, SURF maintain invariance to rotation, scale, and are highly robust in matching problems [22], [23]. After feature detection and description, feature matching and RANSAC filtering, massive high-precision corresponding points can be obtained, most of which distribute at structural areas, like corners, edges, and salient regions, as shown in Fig. 2. Using those correspondences, regions with structural invariant property can be labeled directly. The proportion of matched feature points extracted by SIFT and SURF within each segmented object to the total number of matched feature points is defined as the structural invariant feature

$$S_i = \begin{cases} \frac{N_i}{\max\{N_i | i=1,2,\ldots,n\}} & \exists matched point s in Obj\,(i) \\ 0 & else \end{cases} \quad (1)$$

where, i denotes the ith segmented object, n is the total number of segmented objects, and N_i is the number of correspondences within the segmented object.

Previous works have proved that extracted feature correspondences are positioned mostly sparsely on homogeneous zones [24], and also are affected by the noise and artifacts, such as weak texture, shadows [26]. Although the structural information in HR image is sufficiently detailed, the number and distribution of matched feature points are still insufficient to cover the entire image, limiting the application of feature point matching to CD.

2) Multiscale Dense Matching Feature: The pixel-wise matching result can be generated by dense matching algorithms, which can describe invariant property for every pixel in whole image, and complement insufficient of matched feature points.

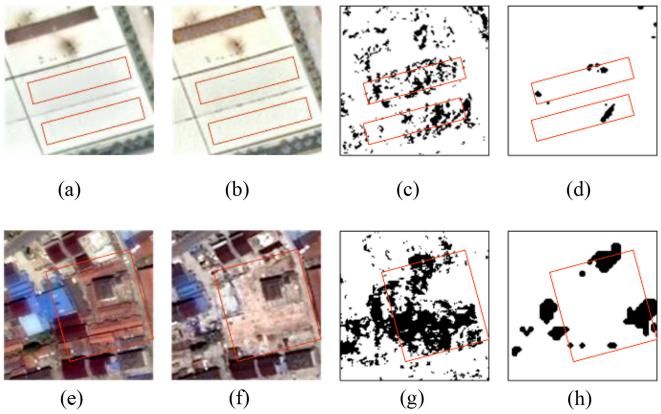

Fig. 3. Dense matching results of ground objects with different geometric sizes at different scales (white regions represent successful matches of SGM, black regions represent failed matches of SGM). (a) Large unchanged objects at T_1. (b) Large unchanged objects at T_2. (c) Results at fine scale. (d) Results at coarse scale. (e) Subtle changed objects at T_1. (f) Subtle changed objects at T_2. (g) Results at fine scale. (h) Results at coarse scale.

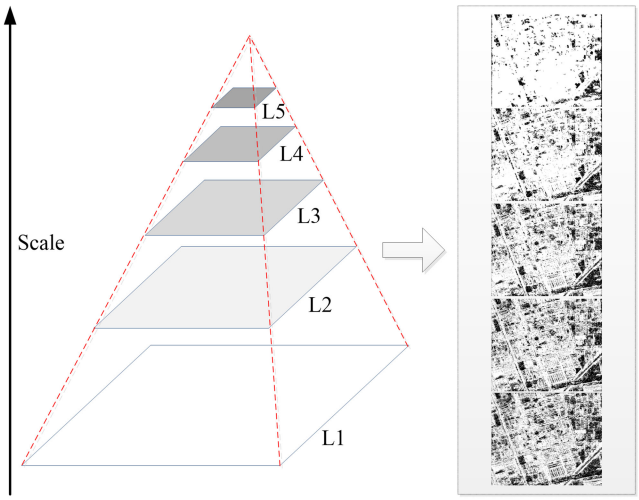

Fig. 4. Multiscale dense matching feature.

As one of the best performance algorithms in dense matching, the semiglobal algorithm (SGM) [59], [60] preserves the advantage of the high efficiency and high precision, and takes census transform [61] as the similarity measurement, which maintains the robustness of the illumination difference. Based on the matching cost, SGM obtains the optimal parallax by minimizing the global energy function, and in the cost aggregation, both the information of the target pixel and the constraint information of surroundings are considered, with postprocessing such as median filtering and left-right consistency check.

However, due to abundant and detailed information of ground objects in HR images, using the single given scale or fixed matching window size in SGM will lead to the dense matching results more fragmented. Moreover, in some large homogeneous areas, the multidirectional matching costs are difficult to transfer into the interior of the object. As shown in Fig. 3(c) , at the fine scale, a large number of mismatches occur due to the similarity of neighborhood information of local windows for large-size ground objects. In contrast, in Fig. 3(h), at the coarse scale, subtle change information will be disturbed by the invariant neighborhood information in the dense matching.

In this article, a multiscale dense matching feature is proposed. First, the pyramid strategy is used to obtain the multiscale images, and then SGM is performed at each layer to obtain the pixel-wise dense matching results, so as to comprehensively reflect the matching properties of ground objects at different scales through the multiscale dense matching feature.

After obtaining dense matching results at every pyramid scale, the segmented objects are used as the analysis unit to calculate the multiscale dense matching feature, which can effectively avoid noise and other interfering information, defined as

$$\mathrm{MSF}_{i,l} = \frac{P_m\,(i,l)}{P_m\,(i,l) + P_u\,(i,l)} \tag{2}$$

where, i represents the ith object and l represents the dense matching scale. P_m is the number of matched pixels in the segmented object, P_u is the number of unmatched pixels.

In the CD process, the dense matching feature obtained by SGM can effectively overcome problems such as weak texture and insufficient spatial distribution of matching points. Furthermore, the multiscale dense matching feature guarantees that the invariant information of large-size unchanged objects can be completely described at the coarse scale, as shown in Fig. 3(d); as well as the subtle change information is not disturbed by the surrounding invariant information at the fine scale, as shown in Fig. 3(g).

3) MultiLevel Matching Feature: Combining the advantages of structural invariant feature and multiscale dense matching feature, the multilevel matching feature is proposed in this article to provide the comprehensive description of the matching properties of ground objects, defined as

$$\mathrm{MLF}_i = \left\{S_i, \mathrm{MSF}_{i,1}, \mathrm{MSF}_{i,2}, \mathrm{MSF}_{i,3}, \cdots\right\} \tag{3}$$

where, i represents the ith object, S_i is the structural invariant feature, $\mathrm{MSF}_{i,l}$ is the dense matching feature at lth scales.

Since structural invariant feature describes the invariant properties at the structural level, multiscale dense features describe the pixel-wise invariant properties at different scales, the proposed multilevel matching features can represent complete invariant properties of ground objects, which can better avoid the false detections caused by differences in imaging conditions.

B. No-Change Sample Extraction Strategy Based on Matching Feature Fusion

Theoretically, the proposed multilevel matching feature are designed on the basis of image matching, which is the process of finding the corresponding points or regions in two images. Therefore, the multilevel matching features could be used directly to extract no-change samples automatically. However, multiscale dense matching features are uncertain for representing the unchanged property within the segmented objects, which lead to difficulties for no-change sample extraction.

To solve this problem, first Gaussian-weighted D–S evidence theory is used to fuse multiscale dense matching features in combination with the information of segmented objects. And then the indicative information from the feature matching obtained by SIFT/SURF is used to further extract regions with explicit structural invariant properties as no-change training samples. The proposed no-change sample extraction strategy can obtain large amounts of accurate no-change samples.

D–S evidence theory is an effective mathematical tool for uncertain modeling and reasoning [62], which can provide explicit estimates of uncertainty between different results from different sources and reduce decision uncertainty. It is widely used in object recognition, data fusion, and decision fusion [43], [63], [64].

In the D–S evidence theory, the discriminative framework Θ is defined, which is a finite set of all possible answers in the question domain. The elements in Θ are mutually exclusive and exhaustive. Proposition A is a nonempty subset of 2^{Θ}, and its basic probability assignment function (BPAF) m: $2^{\Theta} \rightarrow [0, 1]$, representing the degree of belief, and following the constraints:

$$m(\emptyset) = 0, \sum_{A \subset 2^{\Theta}} m(A) = 1. \tag{4}$$

In this article, the discriminative framework for multiscale dense matching feature fusion is constructed as $\Theta = \{C, U\}$, where C and U represent the changes and no-changes, respectively. In this article, the jth matching feature is assigned to the jth evidence for the ith object, $i = 1, 2, \ldots, n$, (where n is the number of segmented objects), and the BPAF is defined as

$$m_{i,j}(U) = \mathrm{MSF}_{i,j}, m_{i,j}(C) = 1 - m_{i,j}(U) \tag{5}$$

where, $\mathrm{MSF}_{i,j}$ denotes the jth scale dense matching feature of the ith object, $m_{i,j}(C)$and $m_{i,j}(U)$ represent the probability of the ith object belonging to C and U, respectively.

However, in the object-based analysis unit, the reliability of matching features of each scale is different and related to the object geometry property. The specific analysis is as follows: For small objects, fine-scale matching results should be selected to avoid the influence of neighborhood noise as shown in Fig. 3(g) and (h). For large objects, coarse-scale matching results should be selected to avoid fragmentation and matching failure as shown in Fig. 3(c) and (d).

Therefore, different weight of evidence should be assigned to reflect the importance of dense matching features at different scales in the discrimination frame. Taking advantages of Gaussian function requiring fewer known parameters and strong descriptive ability, the weight function between the segmented objects and different evidence is established, defined as

$$w_{i,j} = \frac{1}{\sqrt{2\pi}\sigma} \exp\left(-\frac{(j-\mu_i)^2}{2\sigma^2}\right) \tag{6}$$

where, $w_{i,j}$ denotes the assigned weight of the jth evidence in the ith object.

μ_i determines the position of the Gaussian curve center, which is related to the geometry property of the ith object. If the object geometry size is large, the μ_i is assigned to a large value, and the coarse-scale matching feature is selected primarily. If the object geometry size is small, the μ_i is assigned to a small value, and the fine-scale matching feature is selected primarily. Based on the analysis, the relationship between the segmented objects and the most reliable scale can be established.

σ determines the shape of the Gaussian curve, and the shape of the Gaussian curve under different value is shown in Fig. 5. If the σ is set unreasonably, features at other scales cannot be described correctly in the D–S evidence fusion. It is suggested that σ is set ranging from 1.0 to 1.4, which helps to preserve the important matching feature at the most reliable scale and reflect the influence of features at other scales. The weight coefficient is satisfied $w_{i,j} \in [0, 1]$, and the weighted BPAF $m'_{i,j}(C)$ and $m'_{i,j}(U)$ are defined as

$$m'_{i,j}(U) = \frac{w_{i,j}}{\sum_j w_{i,j}} \times m_{i,j}(U), m'_{i,j}(C) = 1 - m'_{i,j}(U). \tag{7}$$

Then, the weighted evidences are combined with an orthogonal sum to synthesize the weighted evidences and obtain the fused results $m_i(C)$ and $m_i(U)$ within each segmented object, defined as

$$\begin{cases} m_i(U) = m'_{i,1} \oplus m'_{i,2} \oplus \ldots \oplus m'_{i,L} = \frac{\prod_{1 \le j \le L} m'_{i,j}(U)}{1 - K_i} \\ m_i(C) = 1 - m_i(U) \end{cases} \tag{8}$$

$$K_i = \prod_{1 \le j \le L} m_{i,j}(C) + \prod_{1 \le j \le L} m_{i,j}(U) \tag{9}$$

where, $m'_{i,j}(U)$ denotes the jth weighted evidence in the ith object for the change class, K is a normalization factor, reflecting the conflict degree of evidences, L is the total number of evidences.

After Gaussian-weighted D–S evidence fusion, the $m_i(U)$ can effectively indicate the no-change possibility of each object, which is normalized to [0, 1]. If the $m_i(U)$ is close to 0, the object is of more possibility to be change class. If the $m_i(U)$ is close to 1, the object is of more possibility to be no-change class.

Furthermore, the structural invariant properties represented by feature point matches are considered. Based on the fused multiscale dense matching results $m_i(U)$, if there are one or more successful matched points in the segmented object, the object is proved it has the invariant structure, and the possibility of no-change class is improved. Therefore, the fused multilevel matching feature F_i can be calculated as follows:

$$F_i = \begin{cases} \|m_i(U), S_i\|_1 & \exists matched\, points\ in\, Obj\ (i) \\ m_i(U) & else \end{cases} \tag{10}$$

where, S_i is structural invariant feature, $\|\|_1$ represents the L1-norm.

As can be seen in Figs. 3(a) and (b) and 6, dense matching features in large-size unchanged ground objects are inconsistent at different scales. With Gaussian-weighted D–S evidence theory, suitable pyramid layer is selected for dense matching feature fusion (large-size ground objects prefer to be expressed

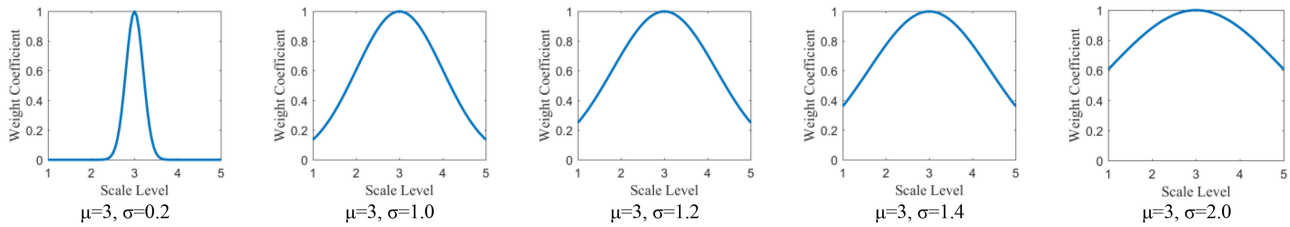

Fig. 5. Gaussian curve at different σ.

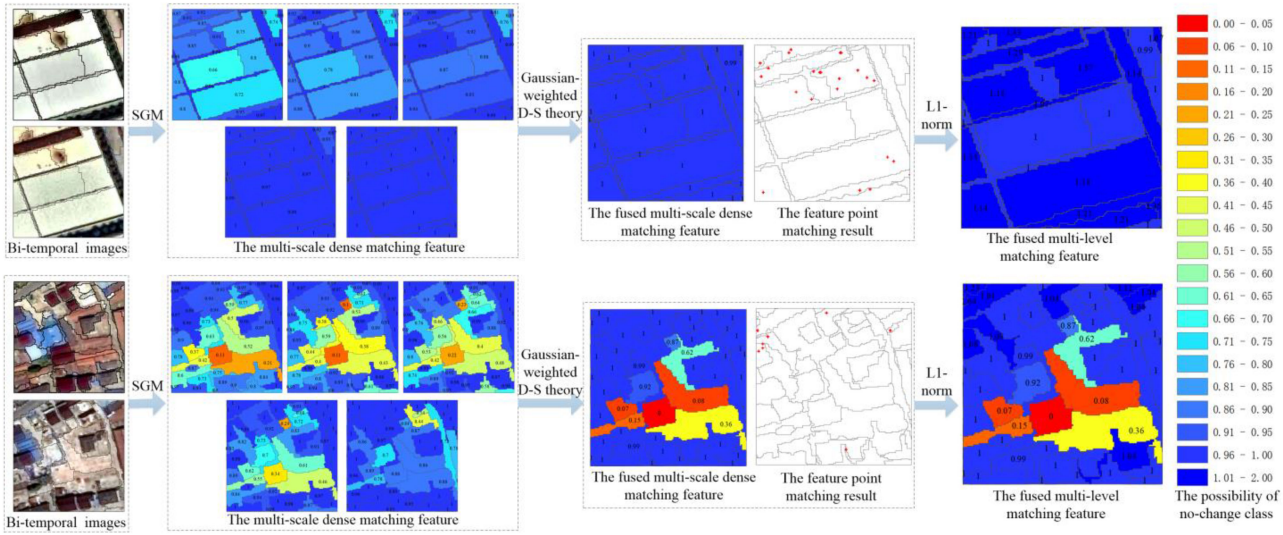

Fig. 6. Fusion process of multilevel matching feature.

at the coarse pyramid scale). Supplemented by point matching features using L1-norm calculation, invariant properties of the larger size unchanged ground objects can be reflected from both scale and structure levels.

As can be seen in Figs. 3(e) and (f) and 6, there are contradictory dense matching features at different scales in the small-size changed ground objects. With Gaussian-weighted D–S evidence theory, the most reliable scale is selected to conduct fusion (smaller-size ground objects prefer to be expressed at the fine pyramid scale). And the results show that the changed properties of the small-size changed ground objects are correctly retained. Supplemented by point matching features using L1-norm calculation, invariant properties of surrounding unchanged objects are also correctly described.

Based on the results of Gaussian-weighted D–S evidence fusion and L1-norm calculation, objects with fused values greater than or equal to 100% will be extracted as no-change samples for the classifier. So, for the fused multilevel matching feature, reliable no-change samples are extracted by setting the threshold T_U ($T_U = 100\%$)

$$\begin{cases} 0 \le F_i < T_U & \text{uncertain sample} \\ F_i \ge T_U & \text{unchanged sample} \end{cases} \tag{11}$$

where, F_i is the fused multilevel matching feature.

It is notable that due to weak textures, occlusions, phenological differences, etc., mismatches occur, resulting in the change samples cannot be extracted directly by fused multilevel matching features.

C. Change Sample Extraction Strategy Based on S^2CVA

There are diverse and complex categories of ground objects in urban areas. And different change types present different geometric patterns, hues, and textures in the images.

Methods using CVA (and its derivatives) for unsupervised CD usually directly distinguish the change from the no-change by magnitude variable [65], [66]. However, a uniform threshold value could make some types of change from being extracted correctly. Therefore, for urban scenes, an automatic sample extraction strategy is proposed in this article. It takes the advantage of S^2CVA to divide different change types by means of direction variables, which can avoid the loss of some subtle changes and extract typical change samples. Then the trained classifier is used to determine the change and no-change categories, instead of directly finding thresholds for separating change from no-change.

First, the difference map is calculated, where $x_{(1)}^B$ and $x_{(2)}^B$ represent the B-dimensional feature maps including spectral and texture features (the mean and variance of the spectrum, the entropy, dissimilarity, contrast, and homogeneity of the GLCM).

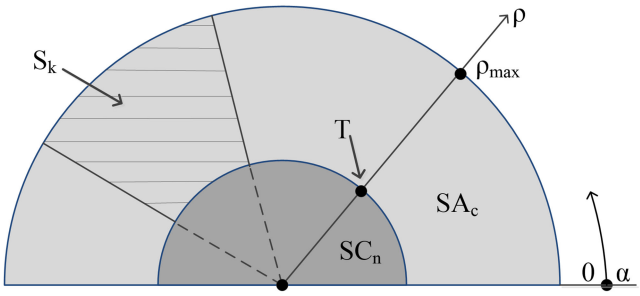

Fig. 7. Multiple changes represented in 2D polar domain by C^2VA [33], [65].

Each feature band is normalized to [0, 1], and the difference map X_D^B is calculated as

$$X_D^B = x_{(1)}^B - x_{(2)}^B. \tag{12}$$

On the basis of difference map, the separability between different change classes can be found in Fig. 7 by calculating magnitude ρ and direction α variables. Specifically, ρ and α are defined as

$$\rho = \sqrt{\sum_{b=1}^{B} \left(X_D^b\right)^2}, \rho \in [0, \rho_{\max}] \tag{13}$$

$$\alpha = \frac{1}{\sqrt{B}} \arccos\left[\left(\sum_{b=1}^{B} \left(X_D^b r^b\right) / \sqrt{\sum_{b=1}^{B} \left(X_D^b\right)^2 \sum_{b=1}^{B} \left(r^b\right)^2}\right)\right], \quad \alpha \in [0, \pi] \tag{14}$$

where, B is the number of difference image bands and the magnitude ρ is calculated by Euclidean distance to indicate the total contribution of the feature bands to the change. $\rho_{\max}$ is the maximum magnitude value and the directional distance α is measured by spectral angle distance (SAD) [67] to indicate the different types of change. r^b is the bth component of the adaptive reference vector, and r is the first eigenvector of the covariance matric A of X_D [33]

$$\mathrm{A} = \mathrm{cov}(X_D) = E\left[\left(X_D - E\left[X_D\right]\right)\left(X_D - E\left[X_D\right]\right)^T\right] \tag{15}$$

where, E[X_D] is the expectation of X_D, the eigendecomposition of the covariance matrix A is defined as

$$\mathrm{A} \cdot \mathrm{V} = \mathrm{V} \cdot \mathrm{W} \tag{16}$$

where, W is a diagonal matrix composed of the sorted eigenvalues in the descending order, V is the eigenvector matrix.

As shown in Fig. 7, in the 2D polar coordinates, segmented objects with higher magnitude values are likely to be changed. And different change types can be separated by the direction variable. Thus, taking advantages of S^2CVA, typical change samples can be extracted in different direction ranges, which can avoid the loss of some subtle changes.

Specifically, segmented objects are divided into g ranges according to the direction variable α, and typical change samples with the magnitude greater than the thresholds T_c are extracted in different direction ranges to train the classifier. Where, T_c is designed as a ratio coefficient representing the proportion of typical change samples occupying in each direction range.

D. Supervised Classifier

To verify the validity and applicability of the proposed features and sample extraction strategy, four representative classifiers (KNN [68], SVM [69], [70], RoF [71], and ExT [72]) proposed in different periods and designed with different principles are selected for experiments. Considering that the extracted samples are correct and representative, which is also small-size, supervised classifiers that can achieve good performance with small training samples are selected to conduct CD work.

The first classifier, KNN, has been first proposed in 1967, which determines the category of the input sample based on the categories of the nearest k samples. In the training stage, it only saves the sample and processes it after receiving the test sample, which requires only a small number of training data and has the advantages of being simple, intuitive, and easy to implement.

The second classifier, SVM, has been proposed in 1995 and constructs the nonlinear decision boundaries between classes directly by defining the separating hyperplane with maximal margin width in feature space. It is widely used in two-group classification in remote sensing and is suitable for small-sample, nonlinear model classification [73].

Compared to single classifiers, ensemble learning can comprehensively take the complementary advantages of multiple classifiers to improve the detection accuracy [74], [75]. We choose two representative classifiers (RoF and ExT) of ensemble learning as the third and fourth classifiers, which have been all proposed in 2006.

RoF can simultaneously encourage the diversity and the individual accuracy of base classifiers within the ensemble through the feature transformation, which has been applied in datasets of different dimensions [15], [71], [76].

ExT uses the entire training set to train the decision trees in the ensemble. It essentially consists of randomizing strongly both attribute and cut-point choice while splitting a tree node, which causes it to be less susceptible to overfitting and can achieve a better performance [72].

III. Experiments

A. Experimental Datasets

In experiment, four datasets have been selected to verify our proposed method, which have been collected from Google Earth with resolution about 0.5 m. The datasets detail information including imaging time, covering location, image size, and sensor source is listed in Table I. In experimental area, Dataset 1 is a large industrial park with diverse and complex internal ground objects changes. Dataset 2 is a dense residential area, where the changes are confused with unchanged backgrounds, making CD more difficult. Dataset 3 is a newly built industrial area with registration errors between the bitemporal images. Dataset 4 is a

TABLE I
DESCRIPTION OF THE DATASET

Dataset	Date	Location	Size(pixels)	Sensor
1	May 2016 - Sep. 2017	Huaian, Jiangsu	3000*2500	P1/ WV-2
2	May 2017 - Aug. 2018	Tianjin	1024*1024	WV-2
3	Apr. 2014 - Apr. 2015	Langfang, Hebei	1600*1600	WV-2
4	Jul. 2016 - May. 2017	Shanghai	17920*7360	WV-3/ P1

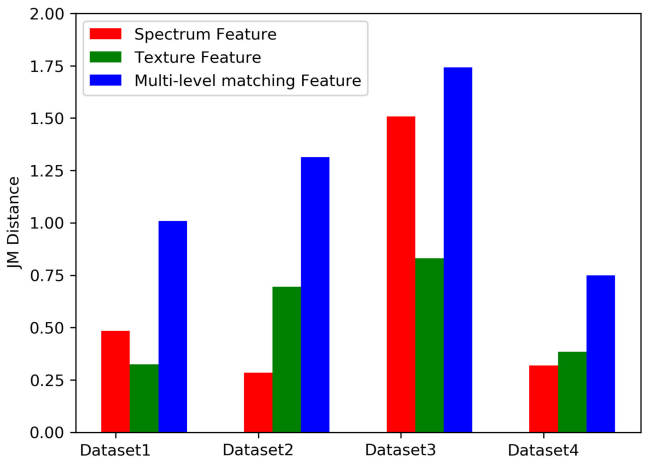

Fig. 8. JM distance with different feature.

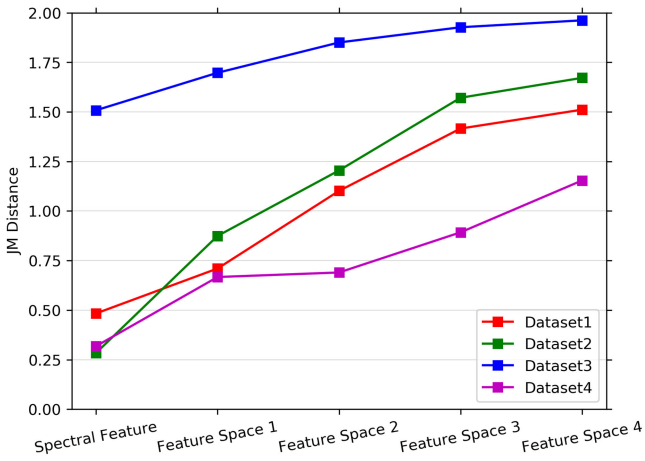

Fig. 9. JM distance with different feature combination.

central town with a large span of change scales, in which change types are diverse and complex.

In order to verify the effectiveness of the proposed framework in this article, comprehensive evaluations have been performed in terms of the following.

1) Separability analysis of different feature combinations to change and no-change classes.
2) Accuracy evaluation of different CD methods for each dataset.
3) Parameter analysis of the proposed CD framework.

Accuracy evaluation indicators include: False alarm rate (FAR), missed alarm rate (MAR), overall accuracy (OA), recall, precision, and Kappa coefficient.

In the segmentation stage, the fractal evolution net approach (FENA) is used, which has been embedded in the eCognition 8.7 software [77]. Where, the shape parameter is set to 0.4 and the compactness parameter is set to 0.5 for all datasets; the scale parameter is set to 50 for Dataset 1,3,4 and 30 for Dataset 2. All these segmentation parameters are determined empirically.

In the sample extraction stage, for Dataset1–3 the parameter T_c is set to 4%, and the parameter g is set to 6. For Dataset 4, the parameter T_c is set to 6%, and the parameter g is set to 9, considering that the changes in Dataset 4 are more diverse and complex.

In the classification process, k is set to 5 for the KNN classifier, the penalty parameter is set to 1, and the radial basis function is used as the kernel function for SVM; the parameter *n_estimators* (the number of base classifiers) is set to 35 for the RoF classifier, and 40 for the ExT classifier; because the processes of industrialization and urbanization are mainly reflected by the transition between construction land and nonconstruction land, and the structural changes within the construction land. This article mainly focuses on the urban changes, hence the areas that are all nonconstruction land in the two period images (with agricultural cultivation and vegetation growth) have been masked and neglected, and the main road with variation of traffic condition in Dataset 2 has been masked and neglected as well.

B. Separability Analysis

In this article, the Jeffries–Matudita (JM) distance [78] is computed to illustrate the effectiveness of the proposed multilevel matching feature in distinguishing between changes and no-changes. The JM distance varies from [0, 2], where 0 means that the two classes are almost completely confused in the feature space, and the value of 2 means that the two classes can be completely separated from each other in the feature space

$$JM = 2\left(1 - e^{-B}\right) \tag{19}$$

$$B = \frac{1}{2}(M_1 - M_2)^T \left[\frac{V_1 + V_2}{2}\right]^{-1} (M_1 - M_2) + \frac{1}{2}\ln\left(\frac{V_1 + V_2}{2\sqrt{|V_1||V_2|}}\right) \tag{20}$$

where, B is Bhattacharyya distance, M_1 and M_2 represent the mean vector of change class and no-change class, respectively.

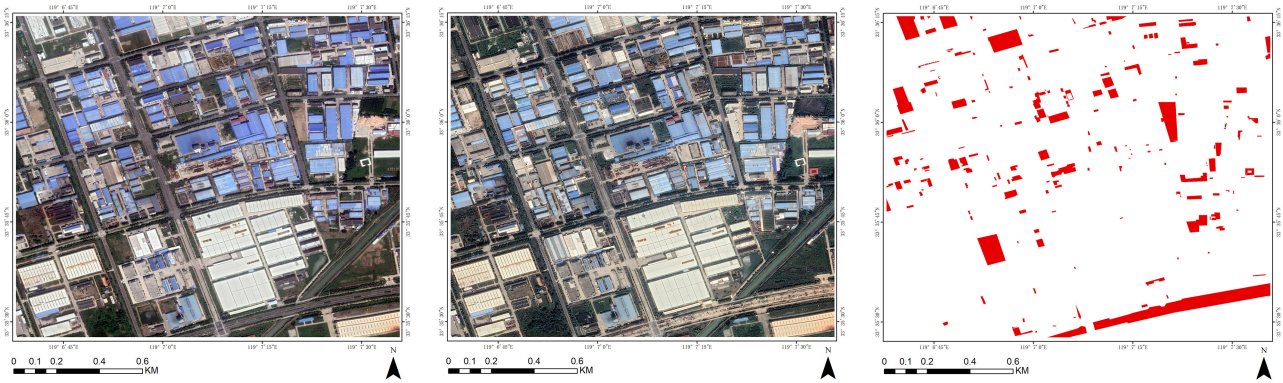

Fig. 10. Bitemporal HR images and reference map of Dataset 1(red regions represent changes).

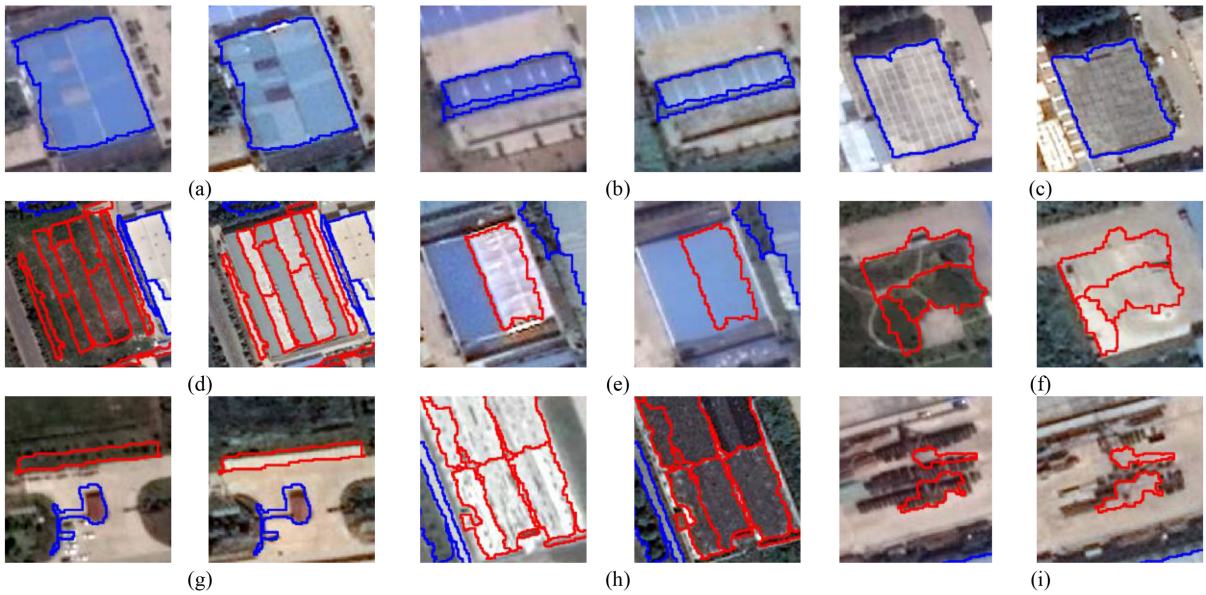

Fig. 11. Distribution of extracted training samples ($T_U = 100\%$, $T_C = 4\%$, and $g = 6$). (a)–(c) No-change samples with spectral variability. (d)–(i) Typical change samples.

V_1 and V_2 represent the covariance matrix of change and no-change classes, respectively.

In order to verify the separability of each feature combinations for the change and no-change classes, the reference maps are used to calculate the JM distances. The JM results are shown in Table II, and displayed in Figs. 8 and 9.

From the JM separability distance results, it can be concluded that only using spectral and texture features cannot effectively distinguish changed ground objects from unchanged objects. With fusing the point feature matching feature, the JM separability distance is improved by 0.02–0.39. Furthermore, with fusing the initial level of dense matching features, the JM separability distance continues to rise by 0.07–0.36. The JM distance is improved by 0.26–0.80 after fusing multilevel matching features. Therefore, the multilevel matching features proposed in this article can effectively improve the separability between the change and no-change classes and help to improve the accuracy of CD.

C. Accuracy Evaluation of Dataset 1

Dataset 1 is located in Huaian city, Jiangsu Province, where ground object changes occur due to factory construction, road maintenance, and temporary material stockpiles, etc. There are diverse types of change with scattering spatial distribution in the region. Due to the differences in imaging time, conditions, and sensors, the spectral variability is obvious in this experimental area. The bitemporal HR images of Dataset 1 are shown in Fig. 10(a) and (b), and the reference map is shown in Fig. 10(c).

Since the multilevel matching feature provides a comprehensive description of the invariant properties of the ground objects from both structure and scale levels, it is robust to illumination difference. Therefore, unchanged objects with spectral variability, as shown in Fig. 11(a)–(c), can be extracted as no-change samples correctly and automatically. The S^{2}CVA method can extract typical types of changes in the experimental area by dividing directions. As shown in Fig. 11(d)–(i), most change types

TABLE II
JM DISTANCES WITH DIFFERENT FEATURE COMBINATIONS, WHERE FEATURE SPACE 1 REPRESENTS THE COMBINATION OF SPECTRAL AND TEXTURE FEATURE. FEATURE SPACE 2 REPRESENTS THE COMBINATION OF FEATURE SPACE 1 AND STRUCTURAL INVARIANT FEATURE

Dataset	Spectral Feature	Texture Feature	Multi-level matching Feature	Feature Space 1	Feature Space 2	Feature Space 3	Feature Space 4
1	0.4835	0.3251	1.008	0.71	1.1016	1.4161	1.5112
2	0.2842	0.6951	1.3131	0.8744	1.2048	1.5713	1.6716
3	1.5081	0.8317	1.743	1.6973	1.8501	1.9268	1.9617
4	0.3183	0.385	0.7493	0.6671	0.69	0.8925	1.154

Feature space 3 represents the combination of feature space 2 and the initial level dense matching feature. Feature space 4 represents the combination of feature space 1 and multilevel matching feature.

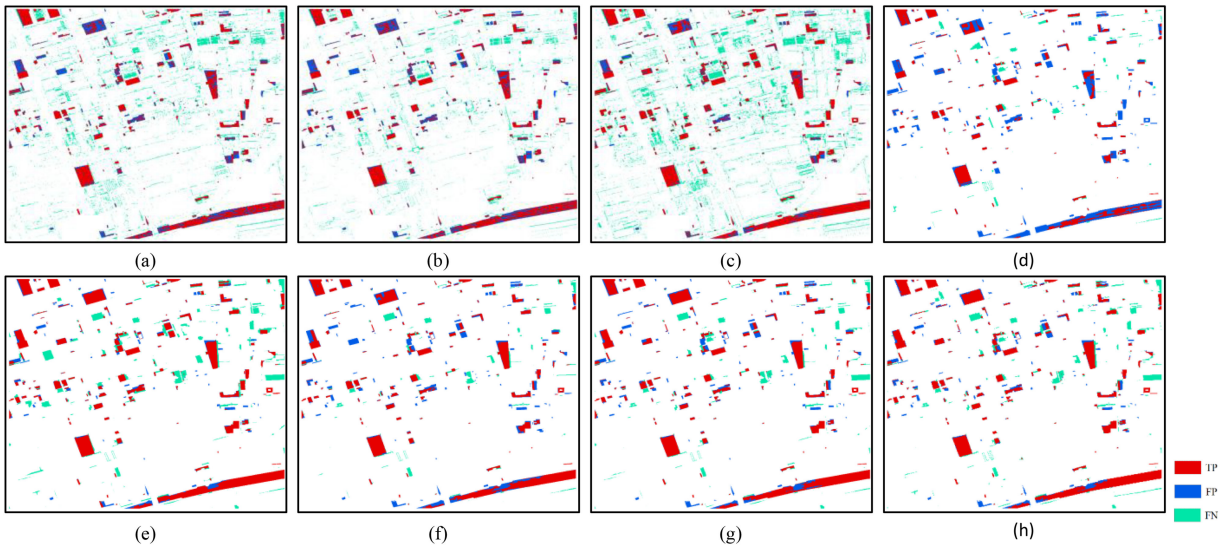

Fig. 12. Confusion Map (Red: TP; Blue: FP; Cyan: FN). (a) PCDA. (b) PCVA. (c) IRMAD.(d) RoF (Feature space 1). (e) RoF (Feature space 4). (f) KNN (Feature space 4). (g) SVM (Feature space 4). (h) ExT (Feature space 4). (Feature space 1 represents the combination of spectral and texture features. Feature space 4 represents the combination of feature space 1 and multilevel matching features).

TABLE III
ACCURACY OF CD BY DIFFERENT METHODS FOR THE DATASET 1 (WHERE FEATURE SPACE 1 REPRESENTS THE COMBINATION OF SPECTRAL AND TEXTURE FEATURE

Method	FAR	MAR	OA	Recall	Precision	Kappa
PCDA	0.0814	0.3254	0.8936	0.6746	0.4854	0.5058
PCVA	0.0561	0.3575	0.9131	0.6425	0.5658	0.5532
IRMAD	0.1265	0.2108	0.8649	0.7892	0.4153	0.4738
RoF (Feature space 1)	0.0133	0.5414	0.9327	0.4586	0.7969	0.5484
RoF (Feature space 4)	0.0428	0.1702	0.9442	0.8298	0.6881	**0.7212**
KNN (Feature space 4)	0.0165	0.3231	0.9521	0.6769	0.8234	**0.7169**
SVM (Feature space 4)	0.0261	0.2582	0.9502	0.7418	0.7642	**0.7252**
ExT (Feature space 4)	0.0318	0.2166	0.9493	0.7834	0.7371	**0.7313**

Feature space 4 represents the combination of feature space 1 and multilevel matching feature).
The bold entities show the experimental results of the proposed change detection framework.

in the sample extraction stage can be identified automatically and participate in the training of the selected classifiers.

Different results of CD methods have been presented in Fig. 12. The three previous figures (a)–(c) are the results using the classical unsupervised pixel-based methods, that are the principal component differential analysis (PCDA) [79], the pixel-based change vector analysis (PCVA) [80], and the iteratively reweighted multivariate alteration detection (IRMAD) [81], respectively. Based on the spectral, texture features, and the extracted samples, Fig. 12(d) shows the CD result obtained

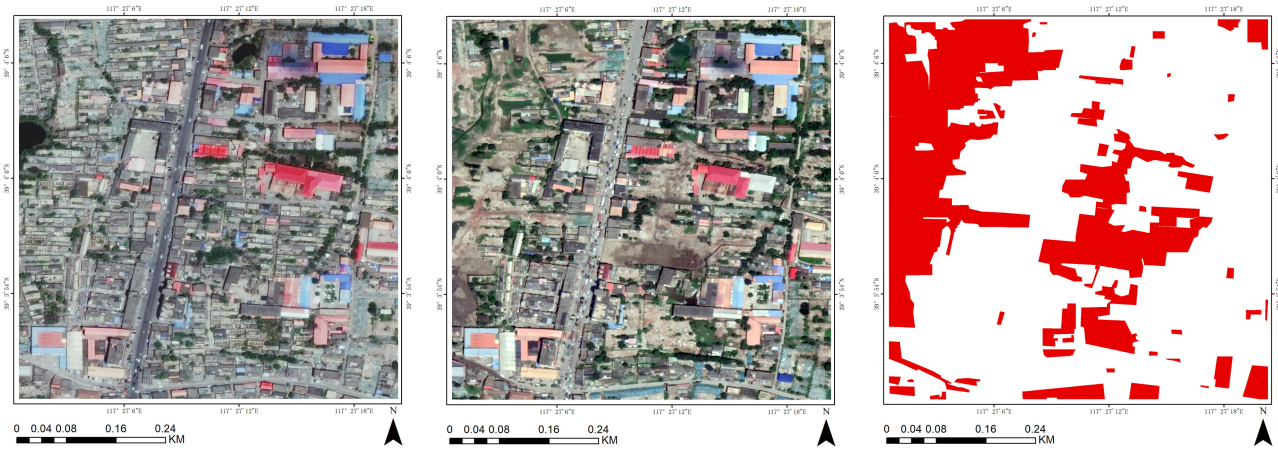

Fig. 13. Bitemporal HR images and reference map of Dataset 2 (red regions represent changes).

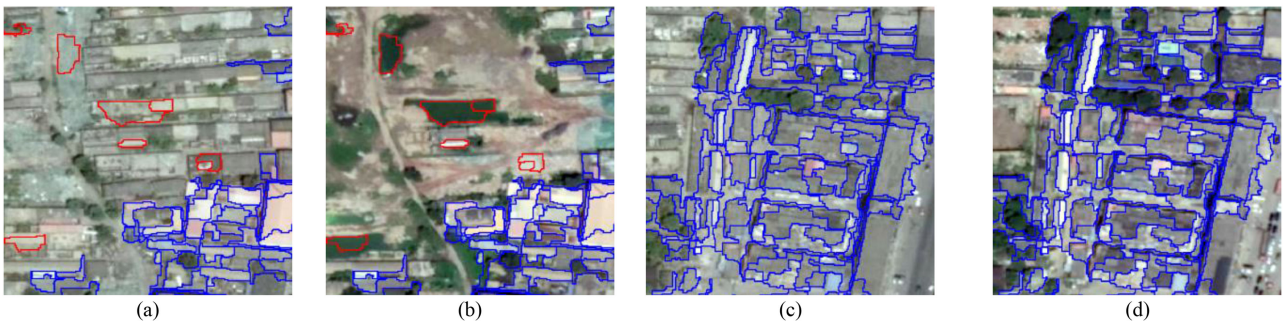

Fig. 14. Distribution of local extracted training samples ($T_U = 100\%$, $T_C = 4\%$, $g = 6$).

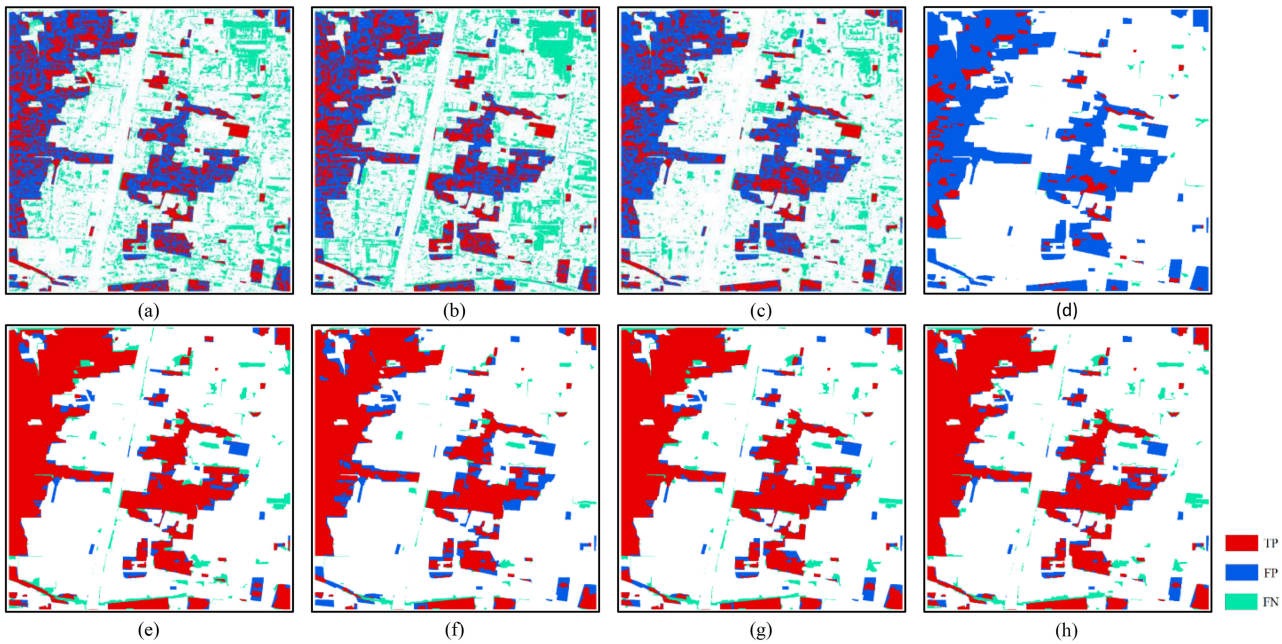

Fig. 15. Confusion Map (Red: TP; Blue: FP; Cyan: FN). (a) PCDA. (b) PCVA. (c) IRMAD. (d) RoF (Feature space 1). (e) RoF (Feature space 4). (f) KNN (Feature space 4). (g) SVM (Feature space 4). (h) ExT (Feature space 4). (Feature space 1 represents the combination of spectral and texture features. Feature space 4 represents the combination of feature space 1 and multilevel matching features.)

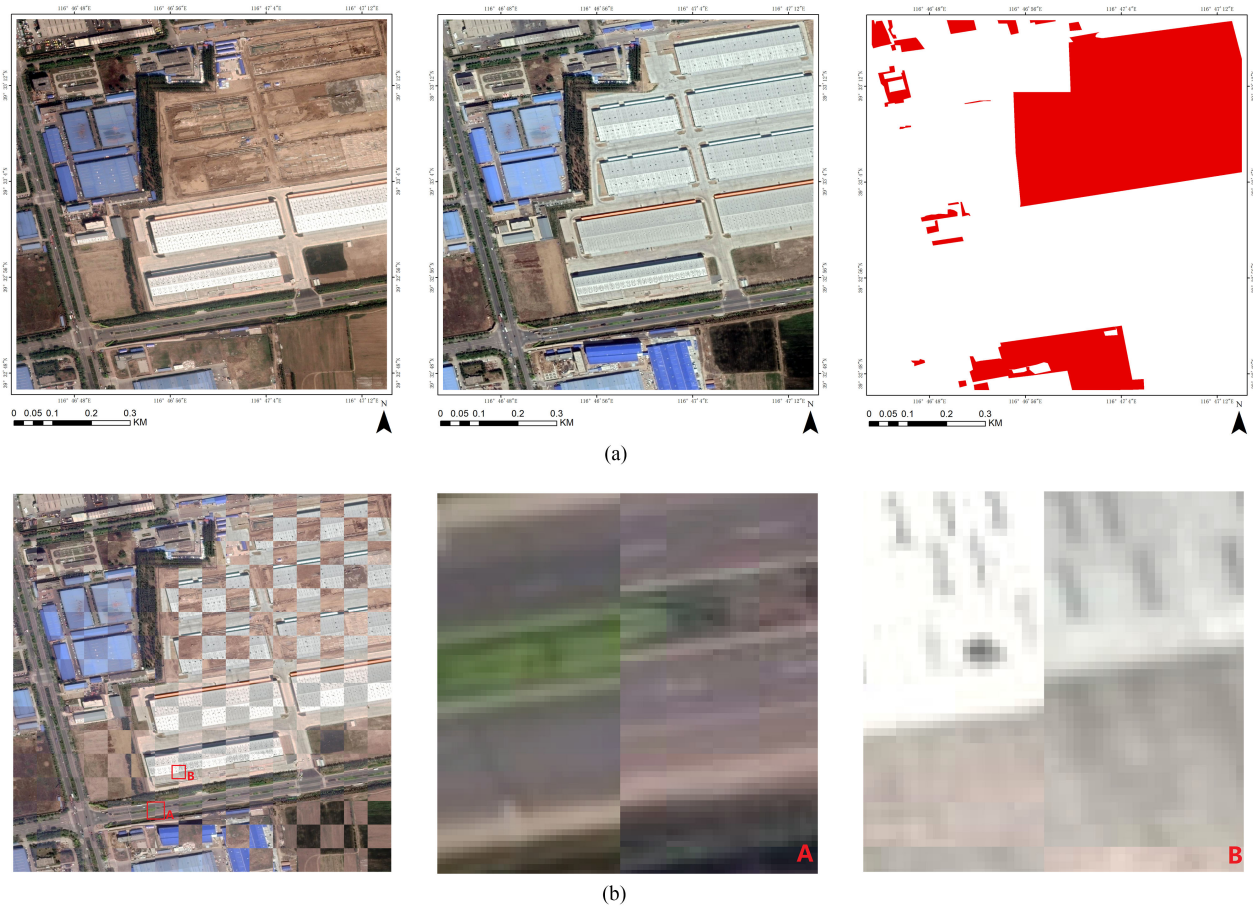

Fig. 16. Dataset 3 (a) Bitemporal HR images and reference map (red regions represent changes). (b) Superposed map of the bi-temporal HR images (showing global and local registration errors).

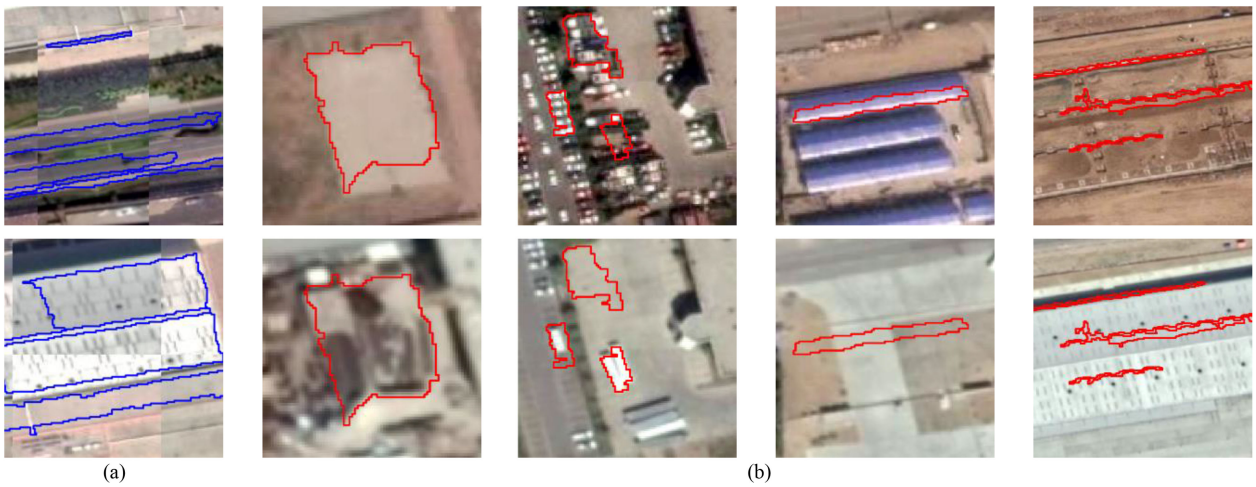

Fig. 17. Distribution of extracted training samples ($T_U = 100\%$, $T_C = 4\%$, and $g = 6$). (a) No-change samples with displacement error. (b) Typical change samples.

by the RoF classifier. Based on the spectral, texture, multilevel matching features, and extracted samples, the later four figures (e)–(h) are the CD results obtained by RoF, KNN, SVM, and EXT, respectively.

It can be observed in Fig. 12(a)–(c) that there are a large number of false alarms and broken edges in the pixel-based CD results. And a lot of missed detections in Fig. 12(d), whereas the later four results perform better and can maintain the edge consistency, which can be seen in Fig. 12(e)–(h).

The accuracy evaluation results of Dataset 1 are listed in Table III. High recall results for the Dataset 1 are obtained from traditional pixel-based methods, but lots of false detections are

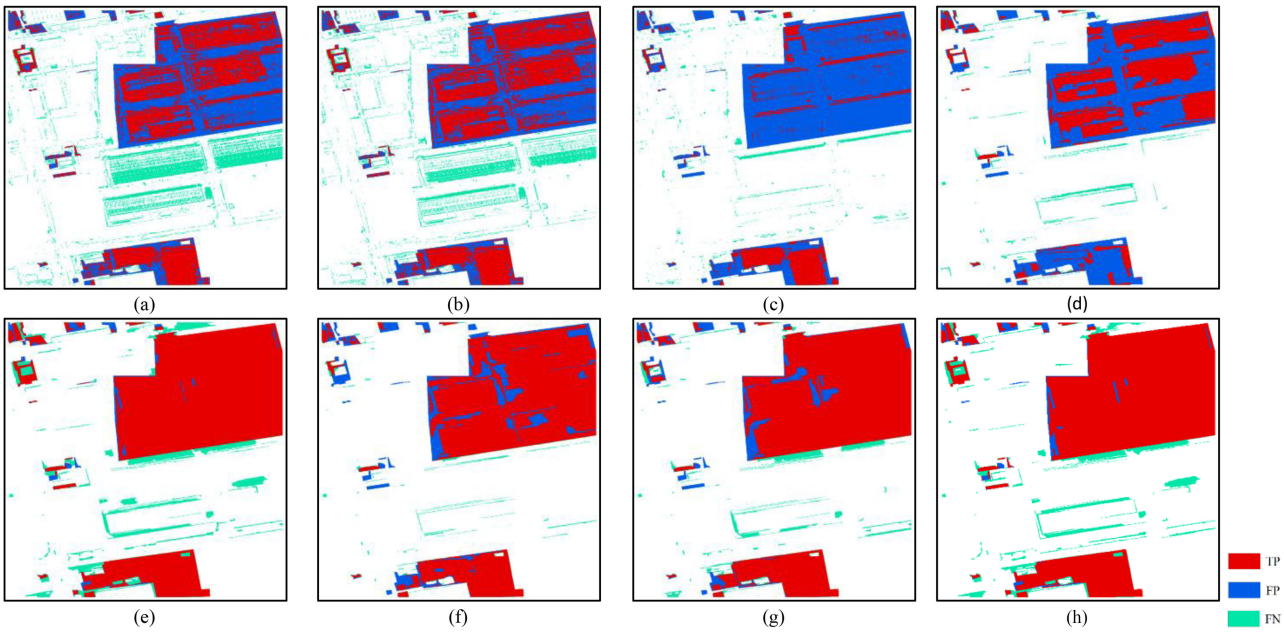

Fig. 18. Confusion Map (Red: TP; Blue: FP; Cyan: FN). (a) PCDA. (b) PCVA. (c) IRMAD. (d) RoF (Feature space 1). (e) RoF (Feature space 4). (f) KNN (Feature space 4). (g) SVM (Feature space 4). (h) ExT (Feature space 4). (Feature space 1 represents the combination of spectral and texture features. Feature space 4 represents the combination of feature space 1 and multilevel matching features).

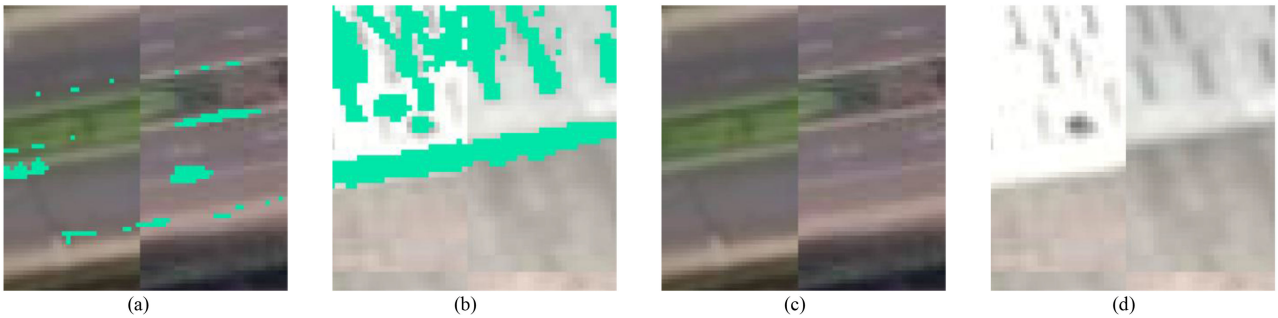

Fig 19. CD results at the edge of roads and houses (a) PCVA. (b) PCVA. (c) SVM. (d) SVM.

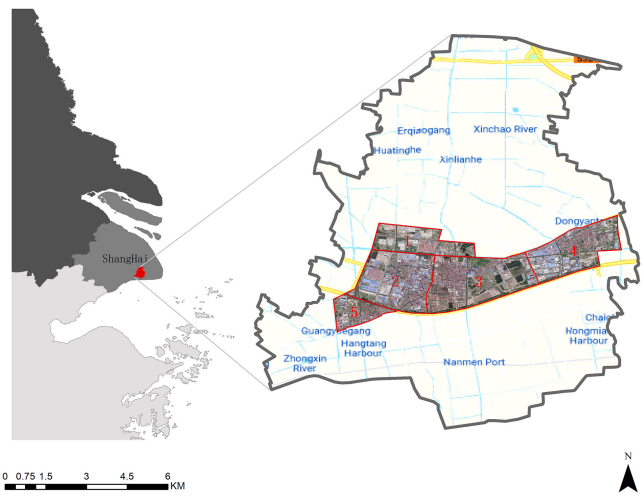

Fig. 20. Location of Dataset 4 (red lines represent the block boundaries).

introduced due to the characteristics of HR data, which lead to the low CD accuracy, whereas the four later results can reduce subtle spurious changes and preserve the object completeness. Furthermore, the proposed features and sample extraction strategy, combined with different supervised classifiers, are effective in reducing false alarms and obtaining better quality CD results.

D. Accuracy Evaluation of Dataset 2

Dataset 2 is located in Tianjin, where changes occur due to residential area deconstruction and some new building constructions. The changed ground objects and unchanged backgrounds appear in similar colors and tones, and it can be seen in the Table II that the separability between the changes and no-changes using only spectral features is 0.2842, resulting in that the two classes are almost completely confused, which makes CD difficult. Fig. 13(a) and (b) show the bitemporal HR images of Dataset 2, and Fig. 13(c) shows the reference map.

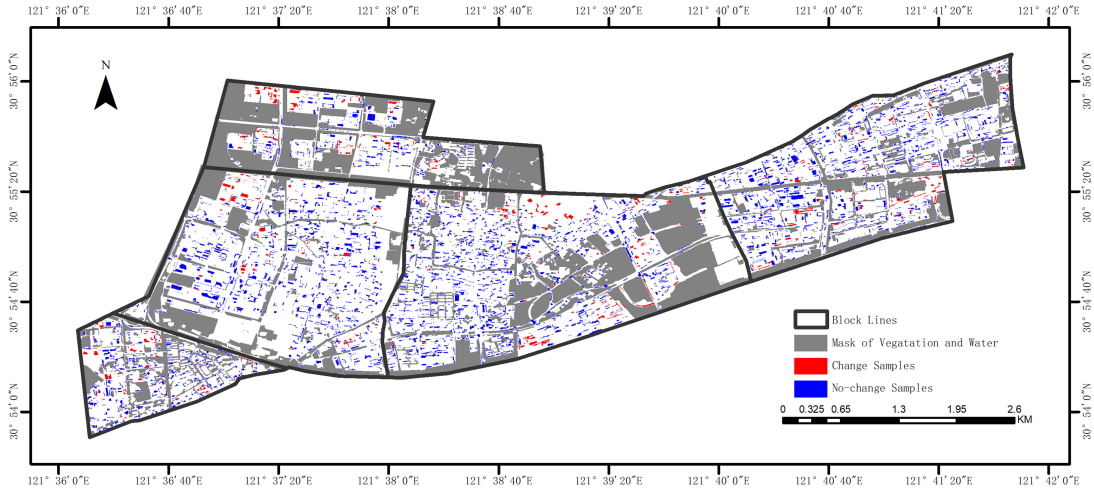

Fig. 21. Distribution of the masked ground objects and verification samples.

TABLE IV
ACCURACY OF CD BY DIFFERENT METHODS FOR THE DATASET 2 (WHERE FEATURE SPACE 1 REPRESENTS THE COMBINATION OF SPECTRAL AND TEXTURE FEATURE

Method	FAR	MAR	OA	Recall	Precision	Kappa
PCDA	0.2237	0.5544	0.6715	0.4456	0.4805	0.2264
PCVA	0.2668	0.5303	0.6497	0.4697	0.4498	0.2006
IRMAD	0.1412	0.6375	0.7015	0.3625	0.5439	0.2431
RoF (Feature space 1)	0.0110	0.8622	0.7192	0.1378	0.8539	0.1636
RoF (Feature space 4)	0.0643	0.1268	0.9158	0.8732	0.8630	**0.8063**
KNN (Feature space 4)	0.0274	0.2410	0.9049	0.7590	0.9279	**0.7691**
SVM (Feature space 4)	0.0554	0.1367	0.9188	0.8633	0.8785	**0.8116**
ExT (Feature space 4)	0.0567	0.1425	0.9161	0.8575	0.8754	**0.8052**

Feature space 4 represents the combination of feature space 1 and multilevel matching feature).
The bold entities show the experimental results of the proposed change detection framework.

To solve the above difficulties, in the proposed sample extraction stage, only regions with strong invariant property in both scale and structure are extracted as no-change samples automatically, and the change samples are extracted by dividing different directions using S^2CVA method to ensure that only high-precision no-change samples and typical change samples are extracted automatically to participate in the subsequent CD.

Different results of CD methods have been presented in Fig. 15. The three previous figures (a)–(c) are the results using the classical unsupervised pixel-based methods, that are PCDA, PCVA, and IMRAD, respectively. Based on the spectral, texture features, and the extracted samples, Fig. 15(d) shows the CD result obtained by the RoF classifier. Based on the spectral, texture, multilevel matching features, and extracted samples, the later four figures (e)–(h) are the CD results obtained by RoF, KNN, SVM, and EXT, respectively.

It is difficult for the classical unsupervised CD methods to detect the changes from the no-changes directly due to the similar spectral statistical information between the changed ground objects and the background. As shown in Fig. 15(d), the result has fewer false alarms, but still have large missed alarms. However, after including the multilevel matching features, it can be seen from Fig. 15(e)–(h) that the CD results can successfully detect the correct change region while reducing false detections.

The accuracy evaluation results of Dataset 2 are listed in Table IV. Due to the similarity spectral between the changed ground objects and the background, in previous three results, the low recall and precision have been obtained by traditional unsupervised CD methods using only spectral information. Whereas in later four results, the recall results obtained by proposed features and training sample extraction strategy are of more than 75%, and the Kappa results of CD combined with the four supervised classifiers are above 76%.

E. Accuracy Evaluation of Dataset 3

Dataset 3 is located in Langfang city, Hebei Province. The bitemporal images of Dataset 3 appear misregistration, projection difference, and shadow, where main changes occur due to some building development and temporary material stockpiles. It can be seen from Fig. 16(b) that there are registration errors between the bitemporal images, especially at the edges of houses and roads. Fig. 16(a) shows the bitemporal HR images and reference map of Dataset 3.

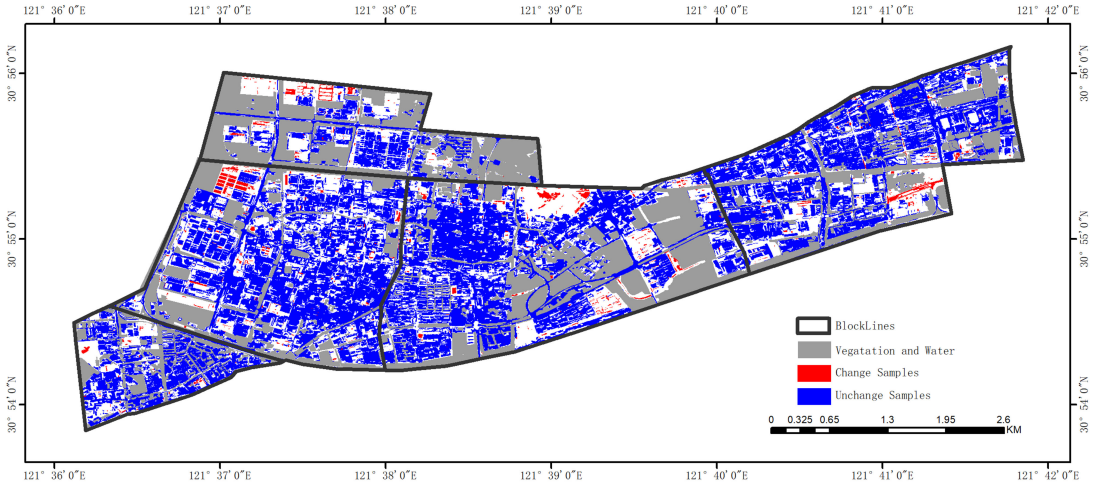

Fig. 22. Distribution of the masked ground objects, change, and no-change training samples ($T_U = 100\%$, $T_C = 6\%$, and $g = 9$).

TABLE V
ACCURACY OF CD BY DIFFERENT METHODS FOR THE DATASET 3 (WHERE FEATURE SPACE 1 REPRESENTS THE COMBINATION OF SPECTRAL AND TEXTURE FEATURE

Method	FAR	MAR	OA	Recall	Precision	Kappa
PCDA	0.191	0.5019	0.681	0.4981	0.6461	0.318
PCVA	0.16	0.4609	0.7161	0.5391	0.7023	0.3928
IRMAD	0.0432	0.811	0.6407	0.189	0.7539	0.1643
RoF (Feature space 1)	0.0354	0.5866	0.7376	0.4134	0.8910	0.4110
RoF (Feature space 4)	0.1242	0.0366	0.9118	0.9634	0.8444	**0.8218**
KNN (Feature space 4)	0.0211	0.1748	0.9156	0.8252	0.9648	**0.8219**
SVM (Feature space 4)	0.0579	0.1057	0.9224	0.8943	0.9154	**0.8393**
ExT (Feature space 4)	0.1111	0.0399	0.9182	0.9601	0.8581	**0.8341**

Feature space 4 represents the combination of feature space 1 and multilevel matching feature).The bold entities show the experimental results of the proposed change detection framewor.

TABLE VI
CD ACCURACY OF EACH BLOCK FOR THE DATASET 4

Accuracy	FA	MA	OA	Recall	Precision	Kappa
Block1	0.1131	0.1625	0.8724	0.8375	0.7535	0.7014
Block 2	0.0299	0.2018	0.9488	0.7982	0.7898	0.7648
Block 3	0.0311	0.0828	0.9613	0.9172	0.8361	0.8520
Block 4	0.0184	0.1694	0.9583	0.8306	0.8916	0.8356
Block 5	0.0100	0.2643	0.9323	0.7357	0.9559	0.7901
Total	0.0009	0.0337	0.9462	0.8369	0.8359	**0.8042**

The proposed multilevel matching features are designed on the basis of image matching, which is the process of finding the corresponding points or regions in two images. Hence the proposed features are not affected by the misregistration, and can be incorporated into the sample extraction strategy. From Fig. 17(a), it can be seen that no-change samples with misregistration can be extracted as training samples correctly and automatically. And from Fig. 17(b), typical change samples can be also extracted by S^2CVA method correctly and automatically.

In Fig. 18(a)–(c), due to misregistration, there are large false detection especially in the classical pixel-based PCDA and PCVA methods. And in the IRMAD result, these unchanged regions with registration errors are detected correctly, but the changes of large building development are still missed. Based on the spectral, texture features, and the extracted samples, Fig. 18(d) shows the CD result obtained by the RoF classifier, which has large missed detections. Based on the spectral, texture, multilevel matching features, and extracted samples, the later four figures (e)–(h) are the CD results obtained by RoF,

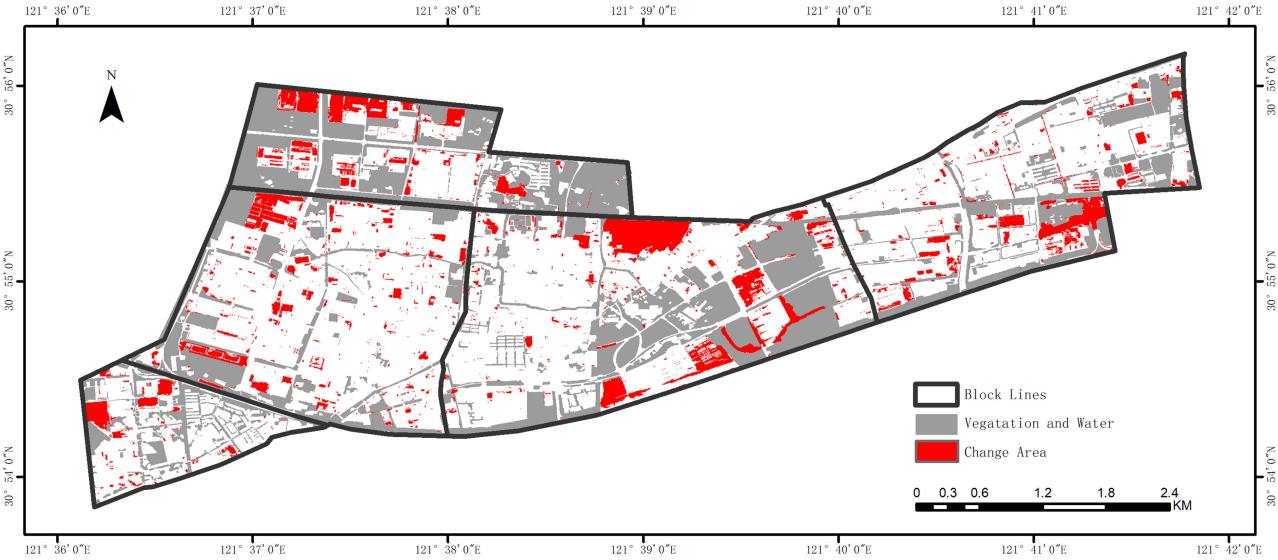

Fig. 23. CD results of Dataset 4 (from RoF classifier).

Fig. 24. Typical change types in Dataset 4. (a) Photovoltaic construction. (b), (c) Industrial park development. (d) Subtle change in industrial park. (e) Large residential area construction. (f) Roof repair. (g) Small residential demolition. (h) Park construction from farmland. (i) Road repair. (j) Temporary material stockpiles.

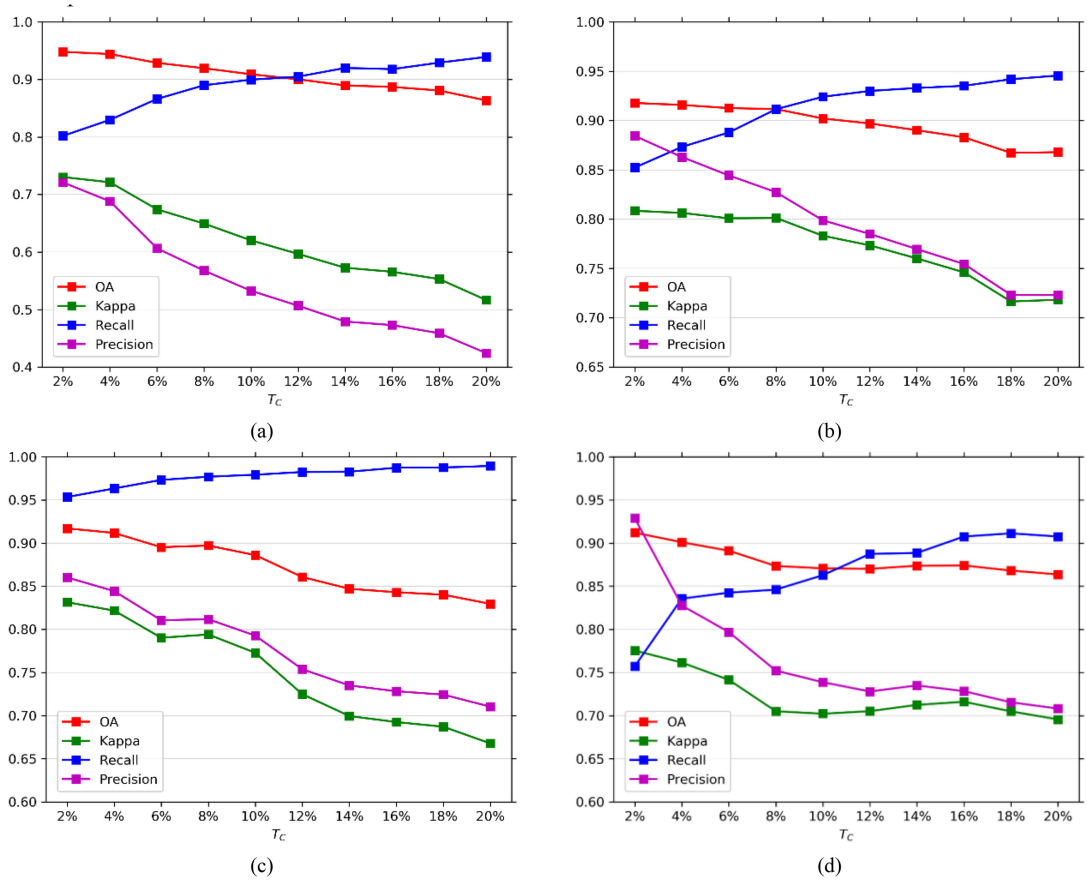

Fig. 25. CD results with different settings of parameter g and T_C. (a) Different T_C in Dataset 1. (b) Different T_C in Dataset 2. (c) Different T_C in Dataset 3. (d)–(h) Different T_C in each block of Dataset 4. (i) Different g for kappa in Dataset 1-3. (j) Different g for kappa in each Block of Dataset 4.

KNN, SVM, and EXT, respectively. In these results, it can be observed that misregistered regions are correctly identified as no-changes [enlarged results are shown in Fig. 19(a)–(d)] and the new constructions of surrounding large buildings are also correctly detected. However, some regions, such as the edges of houses [as shown in Fig. 18(e)–(h)], are still false detected due to the shadows, perspective projections and inconsistency of segmentation.

The evaluation accuracy results are listed in Table V. It can be concluded that the pixel-based methods are affected by misregistration heavily with low recall results. Whereas the proposed features and sample extraction strategy combined with four supervised classifiers perform more accurately with CD recall results exceeding 82% and accuracy results above 84%.

F. Accuracy Evaluation of Dataset 4

In order to verify the applicability of the proposed CD framework for the large spatial extent scene, Dataset 4 is used for experiments. Dataset 4 is located in Fengxian town, Shanghai city, and suited between longitudes 121.60°E and 121.67°E and latitudes 30.90°N-30.93°N, occupying 18.147 km^2. The forms and types of the changed ground objects in this area are diverse and complex, ranging from large-size changes in buildings demolitions/reconstructions, road repairs, etc., to subtle changes, such as roof repairs, temporary material stockpiles, etc. Due to the large coverage area, the study area has been divided into five blocks based on the main road network of the city. In Fig. 20, the red lines represent the block boundaries.

Due to the large extent of Dataset 4, the sampling verification method has been used to evaluate the accuracy of Dataset 4. In each block, approximately 6000 segmented objects have been selected for manual labeling, of which 80% are randomly selected and 20% are subjectively collected to avoid ignoring important change types. The distribution of the masked ground objects (with agricultural cultivation and vegetation growth) and verification samples have been shown in Fig. 21.

The distribution of extracted training samples has been presented in Fig. 22. Taking advantages of ensemble learning, the RoF is chosen to obtain the final CD results for Dataset 4, as shown in Fig. 23, and the typical change types have been presented in Fig. 24. It can be concluded that for complex urban changes, the proposed method can effectively extract different types of changes, such as photovoltaic construction on roofs, large-scale residential area development, road repairs, etc., with low false alarm rate.

The accuracy evaluation results area listed in Table VI for each block. It can be concluded from the results that the recall of each block is above 73%, and the precision of each block is

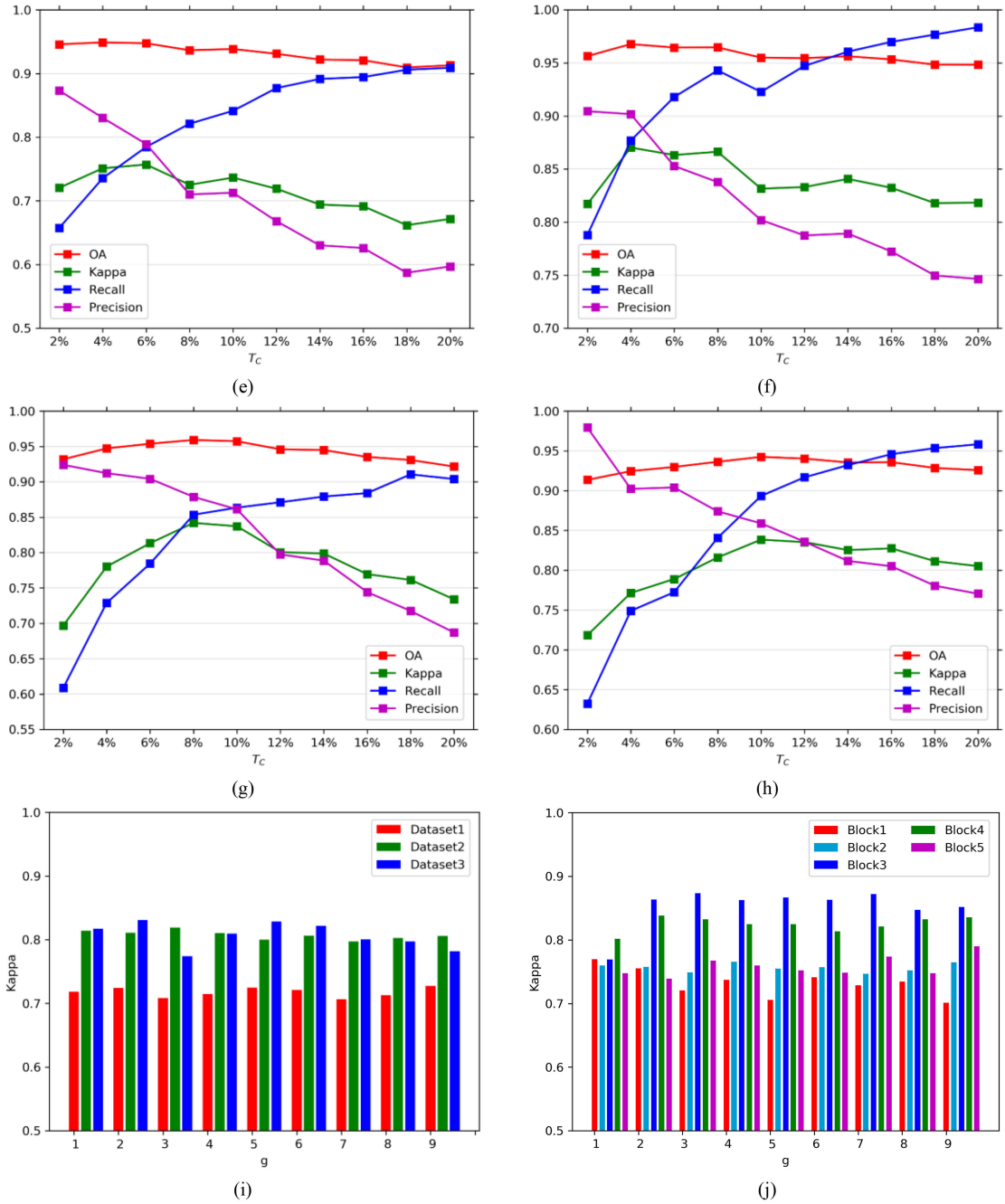

Fig. 25. (Continued).

above 75% with the Kappa above 70%. The overall Kappa of Dataset 4 is 80.42%.

G. Parameter Analysis

The forms and types of the changes in the urban areas are diverse and complex, and the accuracy and representativeness of the extracted training sample have a great influence on the final CD results. In the proposed training sample extraction, the no-change samples are mainly determined by the threshold T_U, and the change samples are mainly determined by the parameters T_C and g, which determine the number and categories of the extracted change samples, respectively. The evaluation accuracy of CD results using different sample extraction parameter setting are obtained for Datasets 1–4, as shown in the following Fig. 25, where the RoF is chosen as the classifier in this experiment.

From Fig. 25(a)–(h), it can be seen that with the increase of T_C, more change samples are extracted to obtain higher recall, but the false alarm rate also increases, leading to worse OA and Kappa results. Therefore, to obtain a higher Kappa for CD, T_C should be set to a smaller value to obtain the most typical change samples.

From Fig. 25(i) and (j), it can be concluded that the CD results are influenced by the number and category of change samples. And compared with the nondirection-divided extraction method, the proposed sample extraction strategy can effectively improve the Kappa of CD for most datasets. However, for different study areas, there are different optimal ranges of direction partitioning.

IV. Conclusion

In this article, we propose a novel urban CD framework that employs multilevel matching features, which can effectively reduce the large number of false detections due to spectral variability, and constructs an automatic sample extraction strategy to improve the CD automation. The proposed multilevel matching features can directly describe the invariant regions at different levels by constructing structural invariant feature and multiscale dense matching feature. Then, an automatic sample extraction strategy is proposed, by which a large number of accurate no-change samples can be extracted by Gaussian-weighted D–S evidence theory and L1-norm, and representative change samples covering different types can be extracted by S^2CVA. The experiments are conducted using four datasets with different CD difficulties, to demonstrate the effectiveness of the proposed framework to spectral variability, spectral confusion between the changed objects and unchanged backgrounds, and misregistration. And the proposed CD method is applicable to a large spatial extent area. Furthermore, due to the merits of the proposed feature and sample extraction strategy, better CD results are obtained using different types of supervised classifiers. However, the proposed CD framework is not applicable to urban areas with high-rise buildings. In addition, for large-scale scenes, how to determine the parameters for sample extraction according to different application scenarios is also a problem to be considered in future research.

References

[1] J. Rogan and D. M. Chen, "Remote sensing technology for mapping and monitoring land-cover and land-use change," *Prog. Planning.*, vol. 61, pp. 301–325, 2004.

[2] C. Gomez, J. C. White, and M. A. Wulder, "Optical remotely sensed time series data for land cover classification: A review," *ISPRS J. Photogrammetry Remote Sens.* , vol. 116, pp. 55–72, Jun. 2016.

[3] K. Y. Wu, X. Y. Ye, Z. F. Qi, and H. Zhang, "Impacts of land use/land cover change and socioeconomic development on regional ecosystem services: The case of fast-growing Hangzhou metropolitan area, China," *Cities*, vol. 31, pp. 276–284, Apr. 2013.

[4] T. Zhang and X. Huang, "Monitoring of urban impervious surfaces using time series of high-resolution remote sensing images in rapidly urbanized areas: A case study of Shenzhen," *IEEE J. Sel. Topics Appl. Earth Observ. Remote Sens.*, vol. 11, no. 8, pp. 2692–2708, Aug. 2018.

[5] Q. H. Weng, "Remote sensing of impervious surfaces in the urban areas: Requirements, methods, and trends," *Remote Sens. Environ.*, vol. 117, pp. 34–49, Feb. 2012.

[6] L. Zhang and Q. H. Weng, "Annual dynamics of impervious surface in the Pearl River Delta, China, from 1988 to 2013, using time series Landsat imagery," *ISPRS J. Photogrammetry Remote Sens.*, vol. 113, pp. 86–96, Mar. 2016.

[7] H. Luo, C. Liu, C. Wu, and X. Guo, "Urban change detection based on Dempster–Shafer theory for multitemporal very high-resolution imagery," *Remote Sens.*, vol. 10, no. 7, Jul. 2018, Art. no. 980.

[8] Z. F. Zheng, J. N. Cao, Z. Y. Lv, and J. A. Benediktsson, "Spatial-spectral feature fusion coupled with multi-scale segmentation voting decision for detecting land cover change with VHR remote sensing images," *Remote Sens.*, vol. 11, no. 16, Aug. 2019, Art. no. 1903.

[9] W. Z. Zhang, X. Q. Lu, and X. L. Li, "A coarse-to-fine semi-supervised change detection for multispectral images," *IEEE Trans. Geosci. Remote Sens.*, vol. 56, no. 6, pp. 3587–3599, Jun. 2018.

[10] Z. Y. Lv, T. F. Liu, C. Shi, J. A. Benediktsson, and H. J. Du, "Novel land cover change detection method based on k-means clustering and adaptive majority voting using bitemporal remote sensing images," *IEEE Access*, vol. 7, pp. 34425–34437, 2019.

[11] C. Wang, H. Liu, Y. Shen, K. G. Zhao, H. Y. Xing, and H. T. Wu, "High-resolution remote-sensing image-change detection based on morphological attribute profiles and decision fusion," *Complexity*, vol. 2020, Mar 2020, Art. no. 8360361.

[12] M. D. Mura, J. A. Benediktsson, F. Bovolo, and L. Bruzzone, "An unsupervised technique based on morphological filters for change detection in very high resolution images," *IEEE Geosci. Remote Sens. Lett.*, vol. 5, no. 3, pp. 433–437, Jul. 2008.

[13] B. Hou, Y. H. Wang, and Q. J. Liu, "A saliency guided semi-supervised building change detection method for high resolution remote sensing images," *Sensors*, vol. 16, no. 9, Sep. 2016, Art. no. 1377.

[14] P. C. Smits and A. Annoni, "Toward specification-driven change detection," *IEEE Trans. Geosci. Remote Sens.*, vol. 38, no. 3, pp. 1484–1488, May 2000.

[15] W. Q. Feng, H. G. Sui, J. H. Tu, W. M. Huang, C. Xu, and K. M. Sun, "A novel change detection approach for multi-temporal high-resolution remote sensing images based on rotation forest and coarse-to-fine uncertainty analyses," *Remote Sens.*, vol. 10, no. 7, Jul. 2018, Art. no. 1015.

[16] T. Leichtle, C. Geiss, M. Wurm, T. Lakes, and H. Taubenbock, "Unsupervised change detection in VHR remote sensing imagery—-An object-based clustering approach in a dynamic urban environment," *Int. J. Appl. Earth Observation Geoinformation*, vol. 54, pp. 15–27, Feb 2017.

[17] Z. X. Li, W. Z. Shi, H. Zhang, and M. Hao, "Change detection based on Gabor wavelet features for very high resolution remote sensing images," *IEEE Geosci. Remote Sens. Lett.*, vol. 14, no. 5, pp. 783–787, May 2017.

[18] M. N. Sumaiya and R. S. S. Kumari, "Gabor filter based change detection in SAR images by KI thresholding," *Optik*, vol. 130, pp. 114–122, 2017.

[19] M. Hussain *et al.*, "Change detection from remotely sensed images: From pixel-based to object-based approaches," *ISPRS J. Photogrammetry Remote Sens.*, vol. 80, no. 2, pp. 91–106, 2013.

[20] X. Wang, S. C. Liu, P. J. Du, H. Liang, J. S. Xia, and Y. F. Li, "Object-based change detection in urban areas from high spatial resolution images based on multiple features and ensemble learning," *Remote Sens.*, vol. 10, no. 2, Feb. 2018, Art. no. 276.

[21] K. Tan, X. Jin, A. Plaza, X. S. Wang, L. Xiao, and P. J. Du, "Automatic change detection in high-resolution remote sensing images by using a multiple classifier system and spectral-spatial features," *IEEE J. Sel. Top ics Appl. Earth Observ. Remote Sens.*, vol. 9, no. 8, pp. 3439–3451, Aug. 2016.

[22] D. G. Lowe, "Distinctive image features from scale-invariant keypoints," *Int. J. Comput. Vis.*, vol. 60, no. 2, pp. 91–110, Nov. 2004.

[23] H. Bay, A. Ess, T. Tuytelaars, and L. Van Gool, "Speeded-up robust features (SURF)," *Comput. Vis. Image Understanding*, vol. 110, no. 3, pp. 346–359, Jun. 2008.

[24] M. T. Pham, G. Mercier, and J. Michel, "Change detection between SAR images using a pointwise approach and graph theory," *IEEE Trans. Geosci. Remote Sens.*, vol. 54, no. 4, pp. 2020–2032, Apr. 2016.

[25] F. Dellinger, J. Delon, Y. Gousseau, J. Michel, and F. Tupin, "Change detection for high resolution satellite images, based on sift descriptors and an a contrario approach," in *Proc. IEEE Int. Geosci. Remote Sens. Symp.*, New York, NY, USA, 2014, pp. 1281–1284.

[26] J. Xing, R. Sieber, and T. Caelli, "A scale-invariant change detection method for land use/cover change research," *ISPRS J. Photogrammetry Remote Sens.,* vol. 141, pp. 252–264, 2018.

[27] P. Coppin, E. Lambin, I. Jonckheere, and B. Muys, "Digital change detection methods in natural ecosystem monitoring: A review," *Int. J. Remote Sens.,* vol. 25, no. 9, pp. 1565–1596, 2004.

[28] D. Lu, P. Mausel, E. Brondizio, and E. Moran, "Change detection techniques," *Int. J. Remote Sens.*, vol. 25, no. 12, pp. 2365–2407, Jun. 2004.

[29] S. Patra, S. Ghosh, and A. Ghosh, "Histogram thresholding for unsupervised change detection of remote sensing images," *Int. J. Remote Sens.,* vol. 32, no. 21, pp. 6071–6089, 2011.

[30] L. Bruzzone and D. F. Prieto, "Automatic analysis of the difference image for unsupervised change detection," *IEEE Trans. Geosci. Remote Sens.*, vol. 38, no. 3, pp. 1171–1182, May 2000.

[31] J. Chen, P. Gong, C. Y. He, R. L. Pu, and P. J. Shi, "Land-use/land-cover change detection using improved change-vector analysis," *Photogrammetric Eng. Remote Sens.*, vol. 69, no. 4, pp. 369–379, Apr. 2003.

[32] J. Chen, X. H. Chen, X. H. Cui, and J. Chen, "Change vector analysis in posterior probability space: A new method for land cover change detection," *IEEE Geosci. Remote Sens. Lett.*, vol. 8, no. 2, pp. 317–321, Mar 2011.

[33] S. C. Liu, L. Bruzzone, F. Bovolo, M. Zanetti, and P. J. Du, "Sequential spectral change vector analysis for iteratively discovering and detecting multiple changes in hyperspectral images," *IEEE Trans. Geosci. Remote Sens.*, vol. 53, no. 8, pp. 4363–4378, Aug. 2015.

[34] S. C. Liu, Q. Du, X. H. Tong, A. Samat, L. Bruzzone, and F. Bovolo, "Multiscale morphological compressed change vector analysis for unsupervised multiple change detection," *IEEE J. Sel. Top ics Appl. Earth Observ. Remote Sens.*, vol. 10, no. 9, pp. 4124–4137, Sep. 2017.

[35] Y. Chen and Z. G. Cao, "An improved MRF-based change detection approach for multitemporal remote sensing imagery," *Signal Process.*, vol. 93, no. 1, pp. 163–175, Jan 2013.

[36] M. Hao, H. Zhang, W. Z. Shi, and K. Z. Deng, "Unsupervised change detection using fuzzy c-means and MRF from remotely sensed images," *Remote Sens. Lett.*, vol. 4, no. 12, pp. 1185–1194, Dec 2013.

[37] T. J. Wu, J. C. Luo, J. W. Fang, J. H. Ma, and X. L. Song, "Unsupervised object-based change detection via a Weibull mixture model-based binarization for high-resolution remote sensing images," *IEEE Geosci. Remote Sens. Lett.*, vol. 15, no. 1, pp. 63–67, Jan. 2018.

[38] F. Pacifici, F. D. Frate, C. Solimini, and W. J. Emery, "An innovative neural-net method to detect temporal changes in high-resolution optical satellite imagery," *IEEE Trans. Geosci. Remote Sens.*, vol. 45, no. 9, pp. 2940–2952, Sep. 2007.

[39] L. Hubert-Moy, A. Cotannec, L. L. Du, A. Chardin, and P. Perez, "A comparison of parametric classification procedures of remotely sensed data applied on different landscape units," *Remote Sens. Environ.*, vol. 75, no. 2, pp. 174–187, Feb. 2001.

[40] D. M. Chen and D. Stow, "The effect of training strategies on supervised classification at different spatial resolutions," *Photogrammetric Eng. Remote Sens.,* vol. 68, no. 11, pp. 1155–1161, Nov 2002.

[41] D. Lu and Q. Weng, "A survey of image classification methods and techniques for improving classification performance," *Int. J. Remote Sens.,* vol. 28, no. 5, pp. 823–870, 2007.

[42] L. Bruzzone and F. Bovolo, "A novel framework for the design of change-detection systems for very-high-resolution remote sensing images," *Proc. IEEE,* vol. 101, no. 3, pp. 609–630, Mar. 2013.

[43] K. Tan, Y. S. Zhang, X. Wang, and Y. Chen, "Object-based change detection using multiple classifiers and multi-scale uncertainty analysis," *Remote Sens.,* vol. 11, no. 3, Feb. 2019, Art. no. 359.

[44] J. F. Liu *et al.*, "SEMI-supervised change detection based on graphs with generative adversarial networks," in *Proc. IEEE Int. Geosci. Remote Sens. Symp.*, New York, NY, USA, 2019, pp. 74–77.

[45] M. C. Li, L. Ma, T. Blaschke, L. Cheng, and D. Tiede, "A systematic comparison of different object-based classification techniques using high spatial resolution imagery in agricultural environments," *Int. J. Appl. Earth Observation Geoinformation,* vol. 49, pp. 87–98, Jul. 2016.

[46] G. D. Guo, H. Wang, D. Bell, Y. X. Bi, and K. Greer, "KNN model-based approach in classification," in *Proc. Move to Meaningful Internet Syst. 2003: Coopis, Doa, ODBASE*, vol. 2888, 2003, pp. 986–996.

[47] I. F. Luque, F. J. Aguilar, M. F. Alvarez, and M. A. Aguilar, "Non-parametric object-based approaches to carry out ISA classification from archival aerial orthoimages," *IEEE J. Sel. Topics Appl. Earth Observ. Remote Sens.,* vol. 6, no. 4, pp. 2058–2071, Aug. 2013.

[48] C. Desir, C. Petitjean, L. Heutte, M. Salaun, and L. Thiberville, "Classification of endomicroscopic images of the lung based on random subwindows and extra-trees," *IEEE Trans. Biomed. Eng.*, vol. 59, no. 9, pp. 2677–2683, Sep. 2012.

[49] G. Mallinis, N. Koutsias, M. Tsakiri-Strati, and M. Karteris, "Object-based classification using Quickbird imagery for delineating forest vegetation polygons in a Mediterranean test site," *ISPRS J. Photogrammetry Remote Sens.,* vol. 63, no. 2, pp. 237–250, Mar. 2008.

[50] X. C. Lu, J. P. Zhang, T. Li, and Y. Zhang, "Hyperspectral image classification based on semi-supervised rotation forest," *Remote Sens.,* vol. 9, no. 9, Sep. 2017, Art. no. 924.

[51] W. Z. Shi, M. Zhang, R. Zhang, S. X. Chen, and Z. Zhan, "Change detection based on artificial intelligence: State-of-the-art and challenges," *Remote Sens.*, vol. 12, no. 10, May 2020, Art. no. 1688.

[52] L. Khelifi and M. Mignotte, "Deep learning for change detection in remote sensing images: Comprehensive review and meta-analysis," *IEEE Access*, vol. 8, pp. 126385–126400, 2020.

[53] A. M. El Amin, Q. J. Liu, and Y. H. Wang, "Convolutional neural network features based change detection in satellite images," *Proc. SPIE*, X. Jiang, vol. 0011, 2016.

[54] S. Saha, F. Bovolo, and L. Bruzzone, "Unsupervised deep change vector analysis for multiple-change detection in VHR images," *IEEE Trans. Geosci. Remote Sens.*, vol. 57, no. 6, pp. 3677–3693, Jun. 2019.

[55] D. F. Peng and H. Y. Guan, "Unsupervised change detection method based on saliency analysis and convolutional neural network," *J. Appl. Remote Sens.*, vol. 13, no. 2, May 2019, Art. no. 024512.

[56] Y. Zhan, K. Fu, M. L. Yan, X. Sun, H. Q. Wang, and X. S. Qiu, "Change detection based on deep Siamese convolutional network for optical aerial images," *IEEE Geosci. Remote Sens. Lett.*, vol. 14, no. 10, pp. 1845–1849, Oct. 2017.

[57] D. B. Mesquita, R. F. dos Santos, D. G. Macharet, M. F. M. Campos, and E. R. Nascimento, "Fully convolutional Siamese autoencoder for change detection in UAV aerial images," *IEEE Geosci. Remote Sens. Lett.*, vol. 17, no. 8, pp. 1455–1459, Aug. 2020.

[58] M. Y. Zhang, G. L. Xu, K. M. Chen, M. L. Yan, and X. Sun, "Triplet-based semantic relation learning for aerial remote sensing image change detection," *IEEE Geosci. Remote Sens. Lett.*, vol. 16, no. 2, pp. 266–270, Feb. 2019.

[59] H. Hirschmuller, "Accurate and efficient stereo processing by semi-global matching and mutual information," in *Proc. IEEE Comput. Soc. Conf. Comput. Vis. Pattern Recognit.*, Eds., vol. 2, 2005, pp. 807–814.

[60] H. Hirschmuller, "Stereo processing by semiglobal matching and mutual information," *IEEE Trans. Pattern Anal. Mach. Intell.*, vol. 30, no. 2, pp. 328–341, Feb 2008.

[61] R. Zabih and J. Woodfill, "Non-parametric local transforms for computing visual correspondence," in *Proc. Eur. Conf. Comput. Vision*, 1994, pp. 151–158.

[62] I. Ruthven and M. Lalmas, "Using Dempster–Shafer's theory of evidence to combine aspects of information use," *J. Intell. Inf. Syst.*, vol. 19, no. 3, pp. 267–301, Nov 2002.

[63] W. Chao, M. Xu, W. Xin, S. Zheng, and Z. Ma, "Object-oriented change detection approach for high-resolution remote sensing images based on multiscale fusion," *J. Appl. Remote Sens.,* vol. 7, no. 1, 2013, Art. no. 073696.

[64] Y. J. Zhang, D. F. Peng, and X. Huang, "Object-based change detection for VHR images based on multiscale uncertainty analysis," *IEEE Geosci. Remote Sens. Lett.,* vol. 15, no. 1, pp. 13–17, Jan. 2018.

[65] F. Bovolo, S. Marchesi, and L. Bruzzone, "A framework for automatic and unsupervised detection of multiple changes in multitemporal images," *IEEE Trans. Geosci. Remote Sens.*, vol. 50, no. 6, pp. 2196–2212, Jun. 2012.

[66] L. Bruzzone and D. F. Prieto, "An adaptive semiparametric and context-based approach to unsupervised change detection in multitemporal remote-sensing images," *IEEE Trans. Image Process. A Publication IEEE Signal Process. Soc.,* vol. 11, no. 4, pp. 452–466, Apr. 2002.

[67] N. Keshava, "Distance metrics and band selection in hyperspectral processing with applications to material identification and spectral libraries," *IEEE Trans. Geosci. Remote Sens.*, vol. 42, no. 7, pp. 1552–1565, Jul. 2004.

[68] T. Cover and P. Hart, "Nearest neighbor pattern classification," *IEEE Trans. Inf. Theory,* vol. 13, no. 1, pp. 21–27, Jan. 1967.

[69] C. Cortes and V. N. Vapnik, "Support-vector networks," *Mach. Learn.,* vol. 20, no. 3, pp. 273–297, 1995.

[70] B. Boser, I. Guyon, and V. Vapnik, "A training algorithm for optimal margin classifier," in *Proc. 5th Annu. ACM Workshop Comput. Learn. Theory*, vol. 5, 1996, pp. 144–152 .

[71] J. J. Rodriguez and L. I. Kuncheva, "Rotation forest: A new classifier ensemble method," *IEEE Trans. Pattern Anal. Mach. Intell.*, vol. 28, no. 10, pp. 1619–1630, Oct. 2006.

[72] P. Geurts, D. Ernst, and L. Wehenkel, "Extremely randomized trees," *Mach. Learn.*, vol. 63, no. 1, pp. 3–42, Apr. 2006.

[73] M. Volpi, D. Tuia, F. Bovolo, M. Kanevski, and L. Bruzzone, "Supervised change detection in VHR images using contextual information and support vector machines," *Int. J. Appl. Earth Observation Geoinformation,* vol. 20, pp. 77–85, Feb. 2013.

[74] M. Skurichina and R. P. W. Duin, "Bagging, boosting and the random subspace method for linear classifiers," *Pattern Anal. Appl.,* vol. 5, no. 2, pp. 121–135, 2002.

[75] R. M. H, D. T, and S. M, "Face detection and sex identification from color images using Adaboost with SVM based component classifier," *Int. J. Comput. Appl.*, vol. 76, no. 3, pp. 1–6, 2017.

[76] J. Xia, P. Du, X. He, and J. Chanussot, "Hyperspectral remote sensing image classification based on rotation forest," *IEEE Geosci. Remote Sens. Lett.,* vol. 11, no. 1, pp. 239–243, Jan. 2014.
[77] M. Baatz and A. Schape, "Multiresolution segmentation: An optimization approach for high quality multi-scale image segmentation," *Angew. Geogr. Info. verarbeitung,* Wichmann-Verlag, pp. 12–23, 2000.
[78] J. Richards and X. Jia, *Remote Sensing Digital Image Analysis*. Berlin, Heidelberg: Springer, 1999.
[79] J. Zhang and Y. Zhang, "Remote sensing research issues of the national land use change program of China," *ISPRS J. Photogrammetry Remote Sens.,* vol. 62, pp. 461–472, 2007.
[80] W. Malila, "Change vector analysis: An approach for detecting forest changes with landsat," *LARS Symposia*, 1980.
[81] A. Nielsen, "The regularized iteratively reweighted MAD method for change detection in multi- and hyperspectral data," *IEEE Trans. Image Process. Publication IEEE Signal Process. Soc.*, vol. 16, no. 2, pp. 463–478, Feb. 2007, doi: 10.1109/TIP.2006.888195.

Yuanxiu Zhou received the B.S. degree from the School of Geography and Information Engineering from China University of Geosciences (Wuhan), Wuhan, China, in 2018, where she is currently working toward the M.S. degree.

Her research interests include high-resolution remote sensing image change detection and image matching.

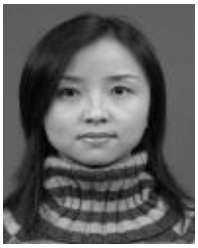

Yan Song received the B.S. Ph.D. degrees in photogrammetry and remote sensing from Wuhan University, Wuhan, China, in 2002 and 2008.

She is currently an Associate Professor with the School of Geography and Information Engineering, China University of Geosciences (Wuhan), Wuhan, China. Her research interests include photogrammetry and remote sensing, multitemporal remote sensing image change detection, remote sensing of islands, and coastal zones.

Songxue Cui received the B.S. degree in marine technology from Tianjin University of Science and Technology, Tianjin, China, in 2006, and the M.S. in cartography and geographical information system from Ocean University of China, Qingdao, China, in 2009.

She is currently an Associate Professor with the National Satellite Ocean Application Service. Her research interests include remote sensing of islands and coastal zones, satellite monitoring of marine disasters.

Haitian Zhu received the B.S. degree in information engineering from Wuhan University, Wuhan, China, in 2003, and the Ph.D. degree in signal and information processing from University of Chinese Academy of Sciences, Beijing, China, in 2015.

He is currently an Associate Professor with the Application Development Department, National Satellite Ocean Application Service. His research interests include remote sensing of islands and coastal zones, and marine remote sensing application.

Jie Sun received the Ph.D. degree in photogrammetry and remote sensing from the Faculty of Remote Sensing and Information Engineering, Wuhan University, Wuhan, China, in 2011.

Since 2011, he is a Lecturer with the China University of Geosciences (Wuhan), Wuhan, China. He has authored or coauthored more than 20 papers. His research interests include remote sensing application for geology, agriculture, and machine learning for object recognition.

Wenjun Qin is currently working toward the B.S. degree with the School of Geography and Information Engineering from China University of Geosciences (Wuhan), Wuhan, China.

His research interests include neural networks and change detection in urban area.